Journal of Great Lakes Research 50 (2024) 102364

Contents lists available at ScienceDirect

Journal of Great Lakes Research

journal homepage: www.elsevier.com/locate/jglr

Modeling attenuation of photosynthetically active radiation across the optical gradient in the Laurentian Great Lakes with application to Lake Erie

Peter J. Alsip [a,*], Mark D. Rowe [a], Alexander Kain [b], Casey Godwin [b]

[a] *Great Lakes Environmental Research Laboratory, National Ocean and Atmospheric Administration, 4840 S. State Rd., Ann Arbor, MI 48108-9719, USA*
[b] *Cooperative Institute for Great Lakes Research, School for Environment and Sustainability, University of Michigan, 440 Church Street, Ann Arbor, MI 48109-1041, USA*

ARTICLE INFO

Communicated by Ram Yerubandi

Keywords:
Photosynthetically Active Radiation
K_d(PAR)
Light attenuation
Suspended sediment model
Aquatic ecological modeling
Biophysical model

ABSTRACT

Representation of subsurface photosynthetically active radiation (PAR) in biophysical models of the Laurentian Great Lakes (LGL) is imperative to their utility as tools for research and management. Here we consolidated measured vertical profiles of subsurface PAR with concurrent water quality (WQ) data from four LGL. We estimated the diffuse attenuation coefficient of PAR (K_d(PAR)) by fitting an exponential function to measured PAR over depth, and evaluated 68 regressions predicting K_d(PAR) as a function of water quality variables (K_d-WQ regressions). We compare four of the top cross-lake calibrated regressions against two published regressions trained on western Lake Erie (WLE) data. Then, as a case study, we demonstrate the utility of our cross-lake calibrated K_d-WQ regressions with a simplified biophysical model of Lake Erie consisting of the Finite Volume Community Ocean Model with submodules for simulating suspended sediment and dissolved organic carbon (FVCOM-SS-DOC). Twenty-five K_d-WQ regressions were identified as candidates for use in biophysical models based on their skill determined via cross-validation. WLE-trained K_d-WQ regressions were less able to simulate K_d(PAR) and PAR in more transparent waters compared to cross-lake calibrated K_d-WQ regressions, which translated to considerable differences in primary production estimates for the central and eastern basins when using WQ data simulated by FVCOM-SS-DOC. A cross-lake calibrated K_d-WQ regression was installed into FVCOM-SS-DOC, which then simulated spatial patterns of suspended sediments and K_d(PAR). These calibrated K_d-WQ regressions can be used in a variety of biophysical models across optically-distinct waters of the LGL to support adaptive management of nutrient inputs and fisheries.

1. Introduction

Light is a fundamental energy source that drives the ecology of aquatic systems. By use of intracellular chlorophyll and other accessory pigments, primary producers are able to capture photosynthetically active radiation (PAR, 400–700 nm) to convert inorganic carbon into carbohydrates and other biomolecules. Light levels influence higher trophic levels in addition to primary producers. For instance, changing light levels can alter the zooplankton community and biomass by influencing bottom-up (i.e., reduction in quantity or quality of algal food, Faithfull et al. (2011)) and top-down controls (i.e., increased light, increased predation, Bramm et al. (2009)). Photosynthesis-irradiance (PI) curves describe the effect of light on primary productivity as a hyperbolic function where photosynthetic rates, as commonly measured by ^{14}C uptake, increase with PAR irradiance towards an asymptote or saturation point after which photoinhibition may occur (Jassby and Platt, 1976). High turbidity increases the attenuation of PAR, which can decrease phytoplankton biomass and primary production (Bramm et al., 2009; Brothers et al., 2017; Ge et al., 2020), alter phytoplankton stoichiometry (Urabe et al., 2002), reduce bottom dissolved oxygen (Moriarty et al., 2021; Pilla and Couture, 2021), and affect predation rates of certain visually-foraging zooplankton and piscivorous fish (Hansen et al., 2013; Jokela et al., 2013; Pangle et al., 2009). The abundance of research in this field makes it apparent that adequately representing PAR is imperative for any aquatic ecosystem model seeking to simulate primary production or higher order ecological processes such as phytoplankton competition and succession (Huisman et al., 2004; Liu et al., 2021), biological drivers of hypoxia (Brothers et al., 2017; Lashaway and Carrick, 2010; Moriarty et al., 2021), secondary production (Bramm et al., 2009; Faithfull et al., 2011), or nutrient cycling and algal

---

* Corresponding author.
E-mail address: peterals@umich.edu (P.J. Alsip).

https://doi.org/10.1016/j.jglr.2024.102364
Received 12 September 2023; Accepted 18 April 2024

stoichiometry (Urabe et al., 2002).

Biophysical models are useful tools for improving our understanding of how physical, biogeochemical and trophic interactions influence aquatic ecosystems. Here, we use the term "biophysical model" to refer to a numerical ocean model linked to a module that simulates advection–diffusion and source-sink terms on one or more state variables representing ecological or biogeochemical quantities. Biophysical models may be formulated with varying degrees of complexity for different applications, ranging from a few to dozens of state variables. Using a biophysical model of Lake Michigan, Rowe et al. (2017) showed that varying mixed layer depth, which affected light limitation of phytoplankton and interaction with benthic filter feeders, was an important driver of primary production. Using a biophysical model of Chesapeake Bay, Moriarty et al. (2021) found that increased light attenuation due to sediment resuspension effected a spatial shift in primary production that also reduced dissolved oxygen up to 2.2 mg L^{-1} in some areas due to changes in photosynthesis and the remineralization rates of organic material. Similar models developed for Lake Michigan (Ji et al., 2002) and the Changjiang Estuary (Ge et al., 2020) have demonstrated how sediment plumes can regulate phytoplankton growth through increased light attenuation and nutrient availability. In Lake Erie, the case study in this manuscript, several biophysical models have provided insights on ecosystem dynamics (e.g. Leon et al., 2011) and key management issues related to harmful algal blooms (Verhamme et al., 2016), hypoxia (Bocaniov et al., 2016; Leon et al., 2006; Rowe et al., 2019), and *Cladophora* (Valipour et al., 2016). Accurate modeling of subsurface light is critical to developing scenarios aimed at resolving nutrient effects on the eutrophication issues facing Lake Erie (Annex 4 Objectives and Targets Task Team, 2015) due to the interactions between light, algal growth, nutrients, and associated eutrophication endpoints.

Attenuation of incident PAR occurs through scattering and absorption by water, suspended particles, and dissolved substances (Abdelrhman, 2017). Changes in subsurface light in coastal zones and lakes are often driven by terrestrial sources of chromophoric dissolved organic material (CDOM) (Gerea et al., 2016; Pilla and Couture, 2021) and suspended sediments (SS), or internal sources such as resuspension of sediment, algal particles, and/or autochthonous CDOM (Niu et al., 2018; Valipour et al., 2017). The intensity of subsurface PAR in aquatic systems has commonly been modeled as an exponential function of depth (Leon et al., 2011; Morel, 1988; Verhamme et al., 2016; Weiskerger et al., 2018):

$$I_z = I_0 \exp(K_d(PAR) \cdot z) \tag{1}$$

$$K_d(PAR) = K_a[SS] + K_b[DOC] + K_c[CHL] + K_w \tag{2}$$

where I_z is irradiance at depth, z is the vertical coordinate (negative downward from the surface), I_0 is surface incident PAR, and K_d(PAR) is the diffuse attenuation coefficient for PAR (Equation (1)), which can be related to the attenuation due to water (K_w) and concentrations of optically-active absorbing and scattering constituents such as SS, dissolved organic carbon (DOC), and chlorophyll-*a* (CHL) with coefficients (K_a,K_b,K_c,K_w) determined by regression (Equation (2)). We recognize that the optical properties of bulk DOC vary depending on the source of DOC and residence time in lakes (Smith et al., 2004); however, CDOM absorption is not often simulated directly in aquatic biogeochemical models, therefore we chose to use DOC to represent CDOM absorption for compatibility with commonly used aquatic biogeochemical models. Absorption and scattering processes (i.e., inherent optical properties, [IOPs]) are wavelength-dependent, and also vary for direct-beam versus diffuse attenuation depending on solar zenith angle (Lee et al., 2005). Spectrally-resolved light attenuation models have been developed that can account for the variable absorption and backscattering of different wavelengths within the PAR spectrum (e.g., Abdelrhman, 2017; Gregg and Rousseaux, 2016; Morel, 1988; Shuchman et al., 2013). Use of complex spectral light attenuation models versus simpler models of diffuse attenuation at a single or binned wavelength may have a negligible or significant impact in aquatic biogeochemical models, depending on latitude, water transparency, model formulations, and uncertainty in other model processes (Gregg and Rousseaux, 2016). In order for spectral light attenuation models to be used for modeling subsurface PAR, IOPs must be defined for the wavelength bands representing the contiguous PAR spectrum; and their calibration requires region-specific spectral observations of subsurface light, while K_d(PAR) may be estimated from more widely available PAR sensor data.

The availability of concurrently measured water quality samples and PAR profiles provides the necessary data for modeling K_d(PAR) as a function of water quality variables (K_d-WQ regressions; Eq. (2)), and K_d-WQ regressions can be used in biophysical models to simulate light attenuation. In the Lake Erie Ecosystem Model (LEEM), K_d(PAR) was estimated as a power function ($y = 0.2273x^{0.734}$) of total suspended solids (TSS) concentration (Limnotech, 2021; Verhamme et al., 2016), whereas Leon et al. (2011) estimated K_d(PAR) from a multiple linear function of SS, algae, DOC, and detritus in their Lake Erie application of the coupled Estuary and Lake Computer Model-Computational Aquatic Ecosystem Dynamics Model (ELCOM-CAEDYM). In their Lake Michigan biophysical model, Rowe et al. (2017) simulated K_d(PAR) as a linear function of chlorophyll and detritus. Lake Erie-specific K_d-WQ regressions have been described in the literature and used in other applications. For their *Cladophora* growth model, Higgins et al. (2005) estimated K_d(PAR) from simple regressions on TSS or turbidity data. Weiskerger et al. (2018) evaluated 23 different regressions using K_d(PAR) and water quality data from the western basin of Lake Erie, 15 of which showed excellent predictive skill ($R^2 > 0.8$). While K_d-WQ regressions have been sufficient in modeling light attenuation in lake-specific or basin-specific applications, there has been little investigation into relationships that could be reliably used in locations with different optical properties within and across the Laurentian Great Lakes (LGL).

In this manuscript we describe the development of K_d-WQ regressions for use in mechanistic ecosystem models of the LGL. We calibrated and assessed various K_d-WQ regressions using a large database of subsurface PAR observations and concurrently-collected water quality data collected from four of the five LGL to identify regressions that can skillfully predict K_d(PAR) across a gradient of optical conditions. We then demonstrated the utility of these regressions in a case study by using them to predict K_d(PAR) and primary productivity using simulated output from a 3D biophysical model of Lake Erie consisting of a hydrodynamic model, SS model, and simplified ecological model. Using the 3D lake model's output, we evaluate the sensitivity of primary production rates to K_d(PAR) prediction between cross-lake calibrated regressions and regressions trained on data exclusively from Lake Erie's western basin. Finally, we install a cross-lake calibrated K_d-WQ regression into the 3D lake model and evaluate the model's ability to recreate spatial patterns of K_d(PAR) in Lake Erie.

2. Methods

2.1. Study area

The geographic scope of our empirical analyses on PAR and WQ spans four of the five LGL including Lakes Michigan, Huron, Ontario, and Erie (Fig. 1a). The LGL are located at temperate latitudes situated along or near the Canadian-US border with trophic statuses ranging from *meso*-eutrophic in some nearshore areas to oligotrophic in the offshore. The LGL are all dimictic, stratifying in the summer and winter and mixing in the spring and late fall. The lakes span a range of water transparency making them a suitable testing ground for light attenuation model development. We also present a biophysical modeling analysis that focuses on Lake Erie (Fig. 1b,c). Lake Erie is the shallowest, warmest, and most productive of the LGL. It is often disaggregated into

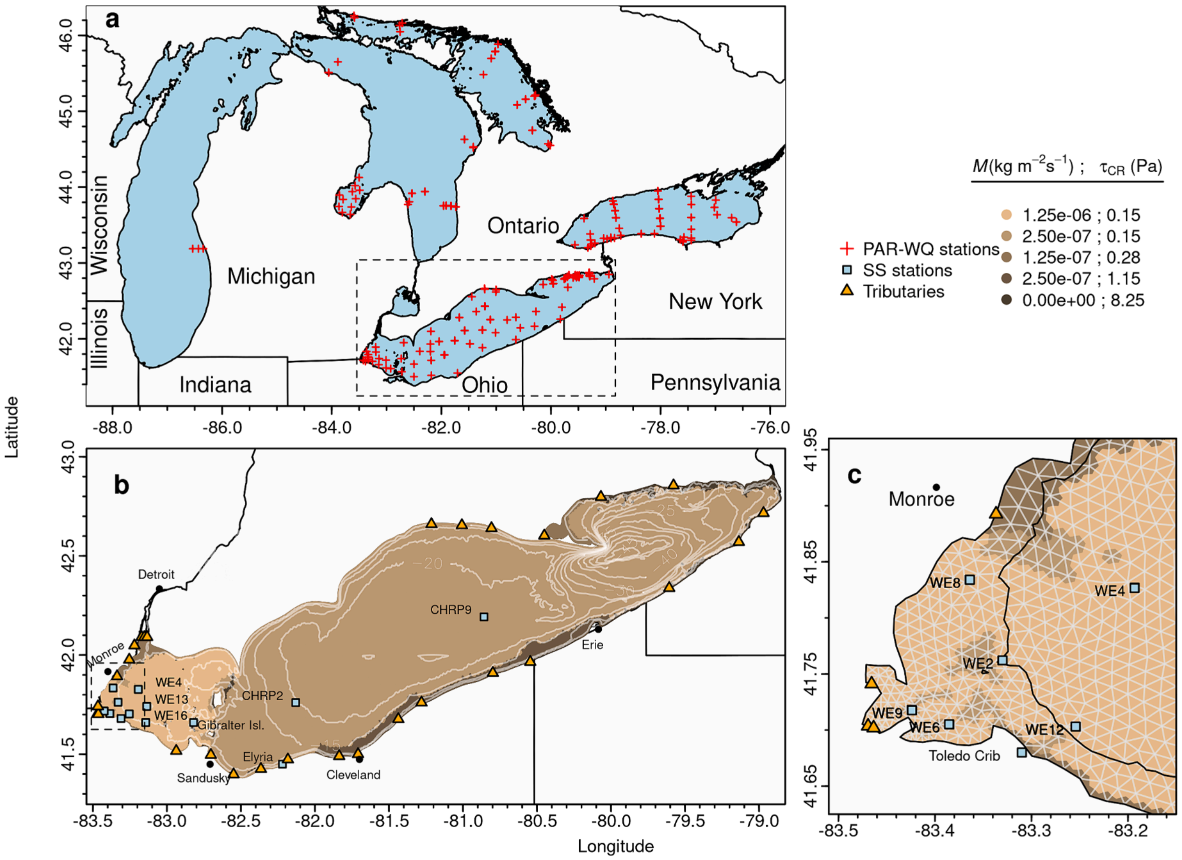

Fig. 1. Sample locations (red crosses) with photosynthetically active radiation (PAR) vertical profiles and associated water quality (WQ) data used to develop light attenuation models (a). Spatial domain (b) and grid (c) of the Lake Erie Finite Volume Community Ocean Model's Suspended Sediment and Dissolved Organic Carbon model (FVCOM-SS-DOC) with suspended sediment sample locations used for calibration and assessment (labeled blue squares), 5 m depth contours, tributary pourpoints (orange triangles), and calibrated erodibility parameters (M, kg m^{-2} s^{-1}; τ_{CR}, Pa). Darker colors indicate less erodible sediment. Cities are indicated as black points.

three subbasins: the western, central, and eastern. Lake Erie has received considerable attention by policymakers, managers, scientists, and the public in recent decades due to the recurring effects of anthropogenic eutrophication such as harmful algal blooms of *Microcystis* in the western basin (Stumpf et al., 2012; Wynne et al., 2011), central basin hypoxia (Stow et al., 2023; Zhou et al., 2013), and nuisance *Cladophora glomerata* in the eastern basin (Higgins et al., 2005).

2.2. Water quality and PAR profile data

We compiled individual profiles of PAR measured using spherical sensors (quantum scalar irradiance) from submersible instruments deployed from research vessels with coincident surface water quality data from various sampling programs across Lakes Erie, Michigan, Ontario, and Huron (Fig. 1a, Electronic Supplementary Material (ESM) Table S1). Water quality data included TSS, DOC, CHL, volatile suspended solids (VSS), and non-volatile suspended solids (NVSS). NVSS is the mineral component of TSS and measured as the residual mass following combustion of TSS at 550° C. VSS is calculated as the difference between gravimetrically-measured TSS and NVSS. The cross-lake dataset included PAR profiles, K_d(PAR) estimates, and water quality data from the Western Lake Erie Monitoring program run by NOAA's Great Lakes Environmental Research Laboratory's (NOAA-GLERL) and the University of Michigan's Cooperative Institute for Great Lakes Research's (CIGLR) (Boegehold et al., 2023; CIGLR and NOAA-GLERL, 2019), the International Field Year for Lake Erie (IFYLE) (IFYLE, n.d.), Environment and Climate Change Canada's (ECCC) Nearshore Nuisance Benthic Algae Dataset in Lake Erie (ECCC, 2012), the Saginaw Bay Multi-stressor study (Stow et al., 2020), the EPA Great Lakes National Program Office's (GLNPO) Lake Erie Dissolved Oxygen Monitoring Program for 2018, and data from the most recent Cooperative Science and Monitoring Initiative (CSMI) field years for Lakes Huron (2017) (Wick et al., in press), Ontario (2018) (Sullivan and Gurdak, 2022), and Michigan (2021). K_d(PAR) data produced by the color-producing agent algorithm (CPA-A) from the Visible Infrared Imaging Radiometer Suite (VIIRs) satellite (NOAA CoastWatch, 2023) in Lake Erie for 2018 were also used to assess K_d-WQ regressions (ESM Table S1). PAR profiles and water quality data were used in four distinct ways:

1. To estimate K_d(PAR) from PAR profiles using equation (1)
2. To develop regressions capable of predicting K_d(PAR) from water quality variables (e.g., equation (2);
3. To assess prediction of subsurface PAR using PAR profiles across lakes Erie, Ontario, Huron, and Michigan; and
4. To assess the performance of selected K_d-WQ regressions when used with a Lake Erie biophysical model for 2018

We applied quality assurance criteria to PAR profiles and concurrently-collected water quality data. PAR profiles were often noisy near the surface due to the instrument interacting with the water surface. We removed PAR measurements within the top 0.5 m of the profile. To focus our analysis on the euphotic zone, we removed all PAR measurements < 0.5 μE m^{-2}s^{-1}. To estimate K_d(PAR), we fit two regressions sequentially. First, we used equation (1) by fitting a linear least-squares regression of log-transformed PAR over depth on the top 5 m of the profile to estimate incident surface PAR (I_0). If I_0 estimates exceeded

3000 μE m^{-2}s^{-1}, the highest intensity expected at the water surface, then they were forced to 3000 μE m^{-2}s^{-1} for the sake of estimating a realistic euphotic zone depth. We then fit equation (1) in the same manner previously described over PAR measurements within the euphotic zone, which ranged from the surface to the depth at which irradiance is equal to 10% of I_0 (Jerome et al., 1983; Lee et al., 2005), to estimate K_d(PAR). K_d(PAR) was averaged across casts for sampling events with replicate casts at the same location and time. Following estimation of K_d(PAR) for each PAR profile, we screened all remaining profiles for quality using a combination of automated screening and visual inspection of the fitted functions. Profiles that lacked concurrent water quality data were removed except the EPA GLNPO DO survey data and NOAA GLERL's and CIGLR's Western Lake Erie Monitoring Program data for 2018, which were used to assess K_d(PAR) prediction using simulated water quality variables and thus did not require concurrent water quality data. Nineteen additional profiles and water quality samples were removed due to influential outliers in TSS, CHL, and K_d(PAR). Twenty-six instances of small-magnitude negative NVSS estimates in the water quality dataset were set to zero so those samples and concurrent profiles in oligotrophic waters would be retained for our analyses. Of the initial 1301 sampling events and 1453 PAR profiles in our cross-lake dataset, we retained 995 PAR profiles from 866 sampling events (129 profiles were replicates); 742 sampling events had concurrent water quality samples sufficient for fitting models and cross-validation, and the other 124 profiles were sufficient for model assessment (ESM Table S1).

Lake Erie made up the majority of the dataset's 866 K_d(PAR) estimates (n = 710, 82% of K_d(PAR) estimates in dataset), followed by Lakes Huron (n = 92, 10.6%), Ontario (n = 57, 6.6%), and Michigan (n = 7, 0.8%) (Fig. 1, ESM Table S1). Lakes Michigan and Huron data were grouped together ("Mich-Huron") in subsequent analyses due to the small amount of Lake Michigan observations and the central and eastern basins of Lake Erie were aggregated into one basin for the purpose of our analyses. Saginaw Bay observations were distinguished from Michigan-Huron observations.

2.3. K_d-WQ regression fitting

We fit 68 regressions to predict K_d(PAR) from CHL, DOC, NVSS, VSS, and/or TSS in R (Version 4.2.3) using ordinary least squares linear regressions, segmented regressions (R package "segmented"), regression trees (R package "rpart"), and power law regressions on up to 742 paired water quality and K_d(PAR) data from the compiled cross-lake dataset. Power laws and linear regressions have been commonly used to relate K_d(PAR) to water quality (Limnotech, 2021; Morel, 1988; Weiskerger et al., 2018). We adjusted predicted K_d(PAR) estimates from the power law models using a retransformation bias correction factor (ε_{adj}) equal to the natural exponent of variance in the residuals (Stow et al., 2006). Segmented regressions fit ordinary least square regressions over two intervals of independent variable data separated by a fitted threshold that maximizes the difference in the predictor's coefficient while ensuring continuity in the predicted relationship. In comparison to ordinary linear regression, segmented regressions can be useful in K_d(PAR) modeling because they may be able to better capture non-linearity in the relationship between K_d(PAR) and water quality as concentrations of optically active constituents approach zero by applying two different slopes based on the concentration of an important predictor (Smith and Baker, 1978). In that sense, it serves as an alternate approach to the power law that is also potentially capable of resolving non-linearity. We evaluated both univariate and multivariate segmented regressions. For multivariate segmented regressions, the segmented predictor variable (i.e., the independent variable with two slopes) was that which produced the largest r^2 when related to K_d(PAR) via simple linear regression. We used 10-fold cross-validation to evaluate model skill in predicting K_d(PAR) outside of the training dataset. Training and testing folds ranged between 543–668 and 58–75 observations, respectively. Model-predicted K_d(PAR) ($\widehat{K_d}$) and observed K_d(PAR) (K_d) were used to calculate root mean square error (RMSE) and the squared Pearson correlation coefficient (r^2_{adj}) adjusted for the number of observations (n) and number of independent variables (p) (ESM Equations S1 and S2). K_d-WQ regressions scoring in the top 50% of RMSE and r^2_{adj} were identified as candidate models that could be used in mechanistic ecosystem models.

We then calculated the relative contribution of each water quality variable to K_d(PAR) using multivariate linear regressions selected from the list of candidate models. This was done by dividing the product of a given predictor's coefficient and concentration by the difference of the predicted K_d(PAR) and attenuation due to water. Contribution of a given water quality variable to K_d(PAR) (K_{wq}) for an individual sampling event was calculated as:

$$\%\ Contribution\ to\ K_d(PAR) = 100\left(\frac{K_{wq}[WQ]}{(K_d(PAR) - K_w)}\right) \tag{3}$$

2.4. Assessment of subsurface PAR prediction with observed water quality

Four of the top performing K_d-WQ regressions from the cross-validation were fit to the entire cross-lake dataset and further evaluated against two published K_d-WQ regressions trained on western Lake Erie data including the top performing multiple linear regression from Weiskerger et al. (2018) which used DOC, NVSS, and CHL as predictors (hereafter referred to as Weiskerger et al., 2018), and a power law function with TSS as the predictor used in the Lake Erie Ecosystem Model (hereafter referred to as LEEM-Kd; Limnotech, 2021; Verhamme et al., 2016). Each K_d-WQ regression predicted the K_d(PAR) from water quality observations and then was input into equation (1) to iteratively calculate PAR at 20 discrete depths across a given profile's euphotic zone. For sampling events with replicate casts, we compared the models' simulated PAR profile against all measured replicate profiles individually. Because the cross-lake dataset lacked PAR measurements at the surface-water interface, we initialized each PAR profile with I_0 estimated from fitting equation (1) to the top 3 m of each PAR profile. The estimated intercept from that regression was input as I_0. In total 683 or 754 profiles of the 995 in the cross-lake dataset were used for this analysis depending on if the K_d-WQ regression used NVSS + VSS or TSS, respectively. We excluded 163–234 profiles due to the absence of data for any required predictor for a given regression; and an additional 78 profiles were excluded due to noisy data in the top 3 m of the profile that reduced our confidence in the resulting estimates of I_0. Model skill in simulating subsurface PAR was determined by comparing simulated PAR for each model at each depth (I^i_{mod}) against the inverse distance weighted value of the two nearest PAR measurements (I^i_{obs}). Model performance was evaluated and compared against each other using several skill metrics including the Nash-Sutcliffe Efficiency (NSE, ESM Equation S3), RMSE, average bias (ESM Equation S4), and relative euclidean distance (relED, Equation S5, Abdelrhman, 2017). RelED was used to convey the ability of each model to recreate an entire profile, as opposed to individual PAR values.

2.5. Lake Erie case study: FVCOM-SS-DOC model structure and assessment

To demonstrate the utility of our cross-lake regressions, we evaluated the skill of four selected cross-lake calibrated K_d-WQ regressions, Weiskerger et al. (2018), and LEEM-Kd in predicting K_d(PAR) given simulated water quality data from a biophysical model of Lake Erie. The

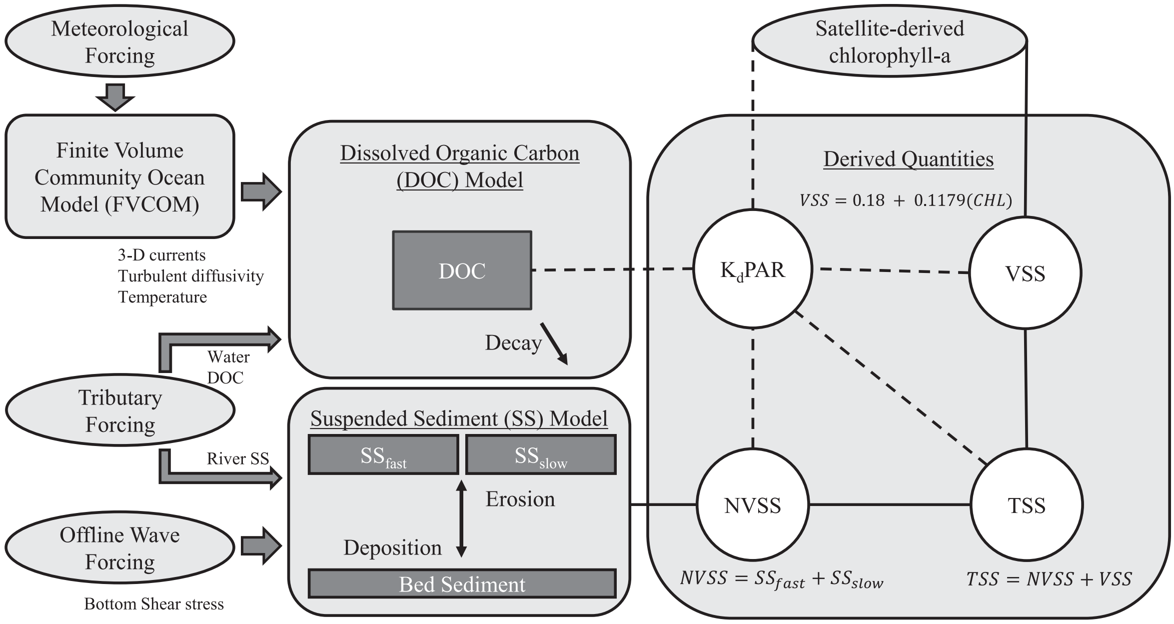

Fig. 2. Process diagram for the 3D biophysical model: the Finite Volume Community Ocean Model's Suspended Sediment and Dissolved Organic Carbon Model (FVCOM-SS-DOC). Light grey ovals indicate external forcings. Rounded, light grey rectangles indicate the three linked models in this framework and the derived variables needed to predict the attenuation coefficient of photosynthetically active radiation (K_d(PAR)). State variables relevant to simulating K_d(PAR) and SS are indicated as dark rectangles. Block arrows show information transfer across modules and external forcings. Sink and .
Source processes for each state variable are directionally indicated by black arrows within each model. White circles represent variables used to predict K_d(PAR) that were derived from external forcings, simulated state variables, or both as indicated by solid black connecting lines. A dashed line indicates whether a given variable could be used in K_d(PAR) prediction

biophysical model consisted of a hydrodynamics model, a SS model, and a simplified ecological model that simulated DOC dynamics. The biophysical model's structure is detailed below.

The Finite Volume Community Ocean Model (FVCOM) version 4.3.1 simulated hydrodynamics and temperature in our Lake Erie biophysical model (Fig. 2). FVCOM is an unstructured grid, finite-volume, free surface, three-dimensional primitive equation ocean model that solves the momentum, continuity, temperature, salinity, and density equations (Chen et al., 2013). Turbulence closure is implemented through the MY-2.5 scheme for vertical mixing (Galperin et al., 1988), and the Smagorinsky scheme for horizontal mixing (Smagorinsky, 1963). The FVCOM application developed for the Lake Erie Operational Forecast System was applied in this study (Anderson et al., 2018; Kelley et al., 2018). Bathymetry was interpolated from the NOAA National Geophysical Data Center (www.ngdc.noaa.gov/mgg/greatlakes/greatlakes.html). Nodes near the Maumee River were deepened to 2 m to satisfy the Courant-Friedrich Levy criterion for ensuring numerical stability under historic peak flow conditions. The unstructured grid consisted of 6,106 nodes and 11,509 elements (Fig. 1). Spatial resolution was typically 2 km mid-lake, transitioning to 0.5 km at the coast, with 20 uniform vertical sigma layers. The grid was refined in regions of interest, including 1.5 km in the western basin and 0.5 km in Maumee Bay and the islands. FVCOM was run from January 1st – December 31st, 2018 using the semi-implicit solver for time integration with a 60 s time step. Temperature was uniformly initialized at 3.45 °C. FVCOM was run with the ice module turned on and ice cover was initialized at 0%, but all analyses were restricted to the ice-free season (April-November) to match the period of observations we used to calibrate K_d-WQ regressions.

We generated meteorological forcing conditions using station-based interpolation methods, using the same methodology as the NOAA Great Lakes Coastal Forecasting System (Beletsky et al., 2003; Schwab and Beletsky, 1998) and Rowe et al. (2019). Hourly wind speed, wind direction, air temperature, dew point temperature, and cloud cover were interpolated over Lake Erie from 37 meteorological stations and 8 National Data Buoy Center buoys (45164, 45169, 45176, 45005, 45165, 45132, 45142, 45167; https://www.ndbc.noaa.gov), when available. Wind speeds were adjusted to 10-m height and empirical relationships were used to adjust land-based meteorological variables for over-lake modification (Beletsky et al., 2003; Schwab and Beletsky, 1998; Rowe et al., 2019).

We used the FVCOM sediment transport module to simulate suspended sediments (FVCOM-SS, Fig. 2). FVCOM-SS is a customizable sediment transport module capable of simulating dynamics of suspended sediments and bedload. This module can be designed to represent spatially-variable sediment bed characteristics and it allows for an unlimited amount of cohesive or non-cohesive suspended sediment state variables. FVCOM-SS also has the ability to resolve sediment stratigraphy and fluid-mud layer effects on bottom boundary layer dynamics, however we did not utilize these features in our application nor did we represent bedload. Our application was entirely focused on SS and was driven by offline outputs from the WaveWatch III model for Lake Erie (Hu et al., 2021). Bottom shear stress (τ_b) is calculated from wave model output and takes into account wave-current interaction in FVCOM's bottom boundary layer module. Erosion rate (E, kg m^{-2} s^{-1}) was modeled as a third-order polynomial (Van Prooijen and Winterwerp, 2010; Equation (4)) with the tunable erosion parameter M (Table S2), which can be modulated by sediment porosity (φ, ESM Table S2), the bed fraction (*BedFrac*, Table S2) of the given suspended sediment variable, τ_b, and critical shear stress (τ_{CR}, ESM Table S2) (Ge et al., 2015; Ge et al., 2020):

$$E = \begin{cases} 0, & \frac{\tau_b}{\tau_{CR}} < 0.52 \\ M(1-\varphi)BedFrac\left(\frac{\tau_b}{\tau_{CR}}\right)^3 + 0.904\left(\frac{\tau_b}{\tau_{CR}}\right)^2 - 0.823\left(\frac{\tau_b}{\tau_{CR}}\right) + 0.204 & \\ M(1-\varphi)BedFrac\left(\frac{\tau_b}{\tau_{CR}} - 1\right), & \frac{\tau_b}{\tau_{CR}} > 1.7 \end{cases} \tag{4}$$

Erosion began once τ_b: $\tau_{CR} > 0.52$, representing incipient mobilization of sediments, and then increased with τ_b according to the third-order polynomial formulation until τ_b: $\tau_{CR} > 1.7$ at which point E increased linearly with τ_b (Van Prooijen and Winterwerp, 2010). Suspended sediments were deposited back to the bed at a constant settling rate for suspended sediment state variables included in the model (W_{SET}, ESM Table S2) and horizontally transported via advection simulated by FVCOM. We included two, non-cohesive SS variables to represent fast-settling (SS_{fast}) and slow-settling sediments (SS_{slow}). The former is intended to be characteristic of coarser sediments while the latter represents finer sediments. We set $W_{SET} = 0.076$ mm/s for SS_{fast}, which was calibrated within a range of 0.03 – 0.95 mm/s reported in the literature (Hawley and Eadie, 2007; Hawley and Lesht, 1992). W_{SET} for SS_{slow} was set to 0.0076 mm/s and the initial bed fractions were calibrated to 0.9 and 0.1 for SS_{fast} and SS_{slow}, respectively. Initial bed fractions were uniformly applied to the entire model domain. In reality, settling velocity will vary with particle diameter and kinematic fluid viscosity (Cheng, 1997) and likely sediment composition as well, but our simplification of two settling rates was sufficient to achieve our objective of simulating aggregate NVSS dynamics in observations following calibration of initial bed fractions. We report on the calibration of erodibility parameters in the results and ESM. For other parameters we did not calibrate, we used Lake Erie-specific values from Valipour et al. (2017) when available (ESM Table S2).

We calibrated the SS model given the influence of SS on K_d(PAR) in Lake Erie (Weiskerger et al., 2018). Because our focus was to resolve subsurface PAR, we aimed to design FVCOM-SS so it could adequately simulate total suspended sediment concentrations near the surface and, thus, calibrated it against NVSS observations collected within the top 1 m of the water column. We calibrated the model against various data types including bias-corrected satellite suspended mineral data, *in-situ* grab sample data of NVSS, and continuous turbidity data converted to an NVSS equivalent (ESM Figure S1). Specifically, we used *in-situ* grab samples from NOAA GLERL and CIGLR's Western Lake Erie Monitoring program (Boegehold et al., 2023; CIGLR and NOAA-GLERL, 2019), continuous turbidity data measured at several locations in the western (CIGLR and NOAA-GLERL, 2019; Ohio State University's Gibraltar Island Buoy: https://seagull-erddap.glos.org/erddap/tabledap/obs_56.html) and central basins (GLERL's Coastal Hypoxia Research Program [CHRP] Mooring data (NOAA-GLERL and CIGLR, 2020; Stow et al., 2023); City of Elyria Water Quality Station: https://seagull-erddap.glos.org/erddap/tabledap/obs_19.html), and the CPA-A product for suspended mineral solids from the VIIRs satellite. We applied a bias-correction to the satellite SS data, which we developed from regressing satellite detected values on corresponding grab samples of NVSS (ESM Figure S2). *In-situ* SS monitoring stations are shown in Fig. 1b-c.

Suspended sediments were also input through 29 pourpoints representing 26 rivers in the model domain (Triangles in Fig. 1, ESM Table S3). Suspended sediment concentrations input from tributaries were taken from the Heidelberg University's National Center for Water Quality Research Tributary Monitoring Program for tributaries covered by that program. We assumed SS coming in from the rivers were 100% NVSS, which is a simplification that we assumed would not greatly impact model skill since wind-wave driven resuspension is the main driver of high turbidity events in Lake Erie (Niu et al., 2018). Extended data gaps in Heidelberg-monitored tributaries were filled using concentration-flow regression trees derived from the tributary-specific Heidelberg data from 2014 to 2019. Regression trees or flow-weighted mean concentrations from nearby tributaries were also used for other tributaries identified as priorities for eutrophication management on the US side of Lake Erie that lacked intensive monitoring during 2014–2019 (i.e. Cattaraugus Creek, Vermilion River, and Grand River, OH) (Annex 4 Objectives and Targets Task Team, 2015). Suspended sediment concentrations for the Detroit River were set to the average bias-corrected concentration detected by VIIRS near the river mouth. Suspended sediment concentrations for all other tributaries were set to flow-weighted mean concentrations calculated by dividing annual load estimates from loading models like the SWAT model (Liu et al., 2016) and the LOADEST model (Robertson et al., 2018) by annual flows. For rivers that lacked sufficient observations of SS to create a tributary-specific concentration estimate, we borrowed estimates from nearby tributaries with sufficient concentration data or loading estimates.

We simulated water quality using the General Ecological Module (GEM) provided with the FVCOM code. GEM is a biophysical modeling framework that can be configured with any number of state variables from functional groups including nutrients, phytoplankton, zooplankton, particulate organic matter, and bacteria (e.g., Rowe et al., 2017; Rowe et al., 2019). We configured GEM to only include DOC (mg L^{-1}) as a state variable and linked it to FVCOM-SS (FVCOM-SS-DOC, Fig. 2) to calculate light attenuation as a function of the water quality variables used in the K_d-WQ regressions. Local DOC source/sink terms include advection and diffusion by FVCOM and a prescribed constant decay rate (2.7×10^{-12} s^{-1}) simulated in the ecological module. DOC was initialized at 2.1 mg L^{-1} across the model grid and input through all rivers at 5.68 mg L^{-1} (Prater et al., 2018), except the Maumee River and Detroit River. The Maumee River's DOC concentration was defined using the average of *in-situ* measurements of DOC at NOAA GLERL's WE2 and WE6 stations and the Detroit River's DOC was set to 2.37 mg L^{-1} (Prater et al., 2018, ESM Table S3). Simulated DOC was compared against surface observations collected by ECCC, the Great Lakes Intake Program, and NOAA GLERL's weekly monitoring program in western Lake Erie from May thru October of 2018. For simplicity in this application focused on calibrating and assessing model components contributing to simulation of subsurface PAR, CHL was prescribed as spatially-variable and temporally-constant concentrations representing the average bias-corrected CHL values from VIIRs between April 1st, 2018 and September 30th, 2018. In future work, the suspended sediment and light attenuation model components can be incorporated into ecological models with dynamic nutrient and chlorophyll concentrations, which was beyond the scope of this study. The bias correction was empirically derived by relating satellite-detected CHL and corresponding *in-situ* extracted CHL (CHL = 0.77[satellite CHL] – 0.495, $r^2 = 0.6$). VSS was estimated from an empirical relationship to CHL derived from Lake Erie data within our cross-lake dataset ($VSS = 0.18 + 0.1179 \cdot CHL$, $r^2 = 0.82$) and added to NVSS simulated by the SS model to estimate TSS.

2.6. Lake Erie case study: Assessment of K_d(PAR) prediction with simulated water quality from FVCOM-SS-DOC and the sensitivity of primary production to K_d-WQ regression

Following calibration of the SS model, we ran FVCOM-SS-DOC for 2018 and used the outputs to predict light attenuation with each of the six aforementioned K_d-WQ regressions at stations in the western and central basins with K_d(PAR) observations. Model skill was reported as NSE.

Using the same biophysical model outputs, we estimated mean daily primary production (PP, mg C m^{-2} d^{-1}) over the year. Mean daily primary production was estimated using K_d(PAR) predicted by each of the six K_d-WQ regressions and the phytoplankton production-irradiance curve from the Great Lakes Primary Production Model (Equation (5)) (Fahnenstiel et al., 1989; Fahnenstiel et al., 2016; Lang and Fahnenstiel, 1996) with the satellite-derived average CHL concentrations used in the biophysical model and PAR irradiance (I) at each of the 20 vertical sigma layer depths (z) as simulated by each of the four cross-lake and two published western Lake Erie K_d-WQ regressions (LEEM-Kd, Weiskerger et al., 2018). In Lake Erie P-I curves, Depew et al. (2006) determined a photoinhibition parameter significantly greater than zero in only 4% of cases, thus we neglected photoinhibition. Primary production was integrated across depths and time (t) to estimate cumulative primary production between April 1st 00:00 GMT and September 30th 23:00 GMT, 2018 (mg C m^{-2}) and then divided by the total number of days in the model run (182.9583) to estimate PP.

$$PP = \frac{\sum_t \sum_z CHL_{z,t} P^B_{max}\left(1-\exp\left(-\frac{\alpha I_{z,t}}{P^B_{max}}\right)\right)\Delta z \Delta t}{182.9583} \tag{5}$$

Maximum photosynthetic rate at light saturation ($P^B_{\max}$, mg C mg $Chl^{-1}h^{-1}$) and the initial linear slope for the P-I relationship at low irradiances (α, mg C mg $Chl^{-1}h^{-1}$) were empirically estimated as functions of temperature at each sigma layer and time step ($T_{z,t}$) and seasonality (Equations 6, 7, ESM Figures S3-S6), respectively, using 12 seasonal mean temperature, $P^B_{\max}$, and α values representing nearshore and offshore for six seasons as reported by Depew et al. (2006) for the eastern basin of Lake Erie:

$$P^B_{\max} = 1.84T_{z,t}^{0.31}, Adjusted\ r^2 = 0.59 \tag{6}$$

$$\alpha = 9.55 + 0.14\cos\left(2\pi\left(\frac{Month}{12}\right)\right) - 3.365\sin\left(2\pi\left(\frac{Month}{12}\right)\right), \quad Adjusted\ r^2 = 0.52 \tag{7}$$

Month was assigned the average month number (0–11 representing December-November) for each season based on the number of sample events that occurred in each month. For example, the winter seasonal mean values reflected two sampling events in March (month number = 3), one in February (month number = 2), and one in December (month number = 0), which translated to an average month number of 2. These empirical relationships and fits are shown in ESM Figures S3-S6. To demonstrate the sensitivity of PP to light prediction, we report the percent difference in primary production estimates derived from the different K_d-WQ regressions relative to one of the top-performing K_d-WQ regressions that was skilled across the gradient of optical conditions in Lake Erie.

2.7. Lake Erie case study: Assessment of simulated spatial patterns of Lake Erie K_d(PAR) against satellite estimates

We then implemented one of the top performing cross-lake calibrated K_d-WQ regressions from our previous analyses in the FVCOM-SS-DOC code and ran it for the entire calendar year of 2018. In this implementation, FVCOM-SS-DOC predicts K_d(PAR) from concurrently simulated and derived water quality variables at each vertical sigma layer. The model then estimates PAR at the bottom of each sigma layer by inputting predicted K_d(PAR) into equation (1) paired with I_0 values, which represents incoming PAR from the previous layer for non-surface layers. For the surface layer, I_0 is provided by the meteorological forcing file created from interpolated observations. We assessed the FVCOM-SS-

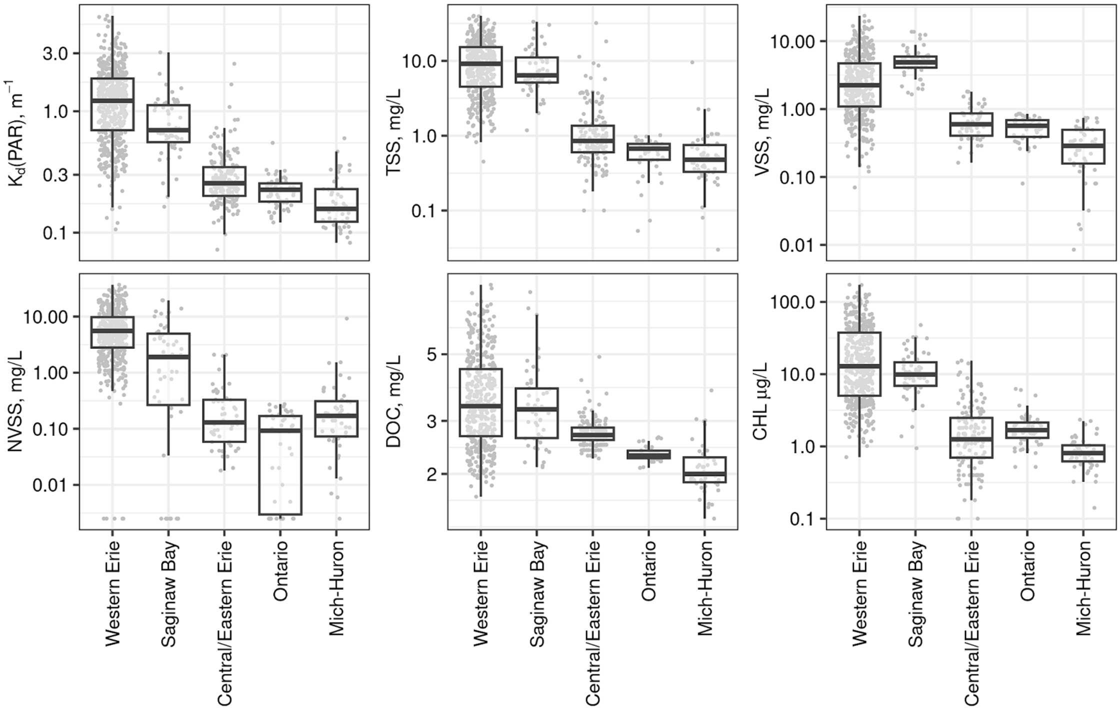

Fig. 3. The distribution of light attenuation and water quality variables included in our cross-lake dataset by basin. Variables include the attenuation coefficient of photosynthetically active radiation (K_d(PAR)), total suspended solids (TSS), volatile suspended solids (VSS), non-volatile suspended solids (NVSS), dissolved organic carbon (DOC), and chlorophyll-*a* (CHL). K_d(PAR) was estimated by fitting an exponential function (equation (1)) to vertical profiles of PAR.

DOC's ability to simulate spatial patterns of K_d(PAR) and compared it against estimates from the CPA-A collected by VIIRs.

3. Results

3.1. Water quality and PAR profile data

K_d(PAR) estimates were derived by fitting equation (1) to vertical profiles of subsurface PAR. On average, equation (1) explained 98% of the variance of subsurface PAR in profiles retained for analyses ($n = 866$). The range of K_d(PAR) values varied by lake and basin (Fig. 3), with 90.3 % of estimates $< 0.3\ m^{-1}$ originating in the more transparent waters of lakes Huron, Michigan, Ontario, and the central and eastern basins of Lake Erie. Conversely, 88.7 % of observations $\geq 0.3\ m^{-1}$ were from the more turbid waters of western Lake Erie and Saginaw Bay. K_d(PAR) estimates from the *in-situ* cross-lake dataset ranged from 0.072-6.1 m^{-1} with a median of 0.70 m^{-1} and mean (±sd) of $1.0 \pm 0.90\ m^{-1}$ ($n = 866$, Fig. 3). The coefficient of variation (CV) of K_d(PAR) for each basin was as follows: 78% (central/eastern Erie), 66.2% (western Erie), 59% (Saginaw Bay), 54.2% (Mich-Huron), and 30% (Ontario). CV across the entire dataset was 90 %. Water quality variables also varied by lake and basin (Fig. 3). Western Lake Erie had the highest median concentrations of all water quality variables except VSS, which was highest in Saginaw Bay with a median concentration of 4.87 mg L^{-1}. Lakes Michigan, Huron, Ontario, and the central and eastern basins of Lake Erie had similar concentrations for all water quality variables. Western Lake Erie and Saginaw Bay were the only basins with TSS, VSS, and NVSS medians greater than 1 mg L^{-1} and average CHL greater than 10 ug L^{-1}. Across the entire dataset, variability in water quality concentrations relative to their mean values was similar for TSS (CV = 1.04), VSS (CV = 1.14), NVSS (CV = 1.16), and CHL (CV = 1.52). Dissolved organic carbon had the smallest variability relative to its mean (CV = 0.37).

3.2. K_d-WQ regression fitting

We assessed a total of 68 K_d-WQ regressions (ESM Figure S7). The number of K_d(PAR) estimates used in the cross-validation varied between 610–742 depending on the number of available observations of the independent variables. The abundance of western Lake Erie data in our dataset may bias the evaluation of K_d-WQ regressions towards those most capable in that basin. To compensate, we report model RMSE at lower K_d(PAR) values typical in non-western Lake Erie waters (K_d(PAR) $< 0.3\ m^{-1}$) to show which regressions have utility in more transparent waters. There were 27 K_d-WQ regressions that scored above the median r^2_{adj} and RMSE when predicting across the entire data range and also scored above the median RMSE when predicting across K_d(PAR) $< 0.3\ m^{-1}$ (ESM Table S4, Figure S8). Two regression trees were initially included in the list of top regressions, but additional inspection of prediction-observation comparisons indicated these regressions were not capable of predicting K_d(PAR) $< 0.3\ m^{-1}$ and were removed from the list of regressions reported in ESM Table S4.

The resulting 25 K_d-WQ regressions with the greatest skill consisted of 10 multiple linear regressions, 10 segmented multiple linear regressions, and 5 power law regressions (ESM Table S4, Figure S8). The linear regression using VSS, NVSS, DOC (all in mg L^{-1}), and CHL (ug L^{-1}) as predictors was most accurate in predicting K_d(PAR) (Table 1) followed by several other multiple linear regressions and segmented regressions. The difference among the candidate regressions' r^2_{adj} and RMSE values was small. The segmented regressions on VSS + NVSS + DOC + CHL, NVSS + DOC + CHL, and power laws on TSS + DOC and TSS + DOC + CHL were among the most skilled of their respective forms (ESM Table S4, Figures S7-S8). Multivariate linear regressions, segmented regressions, and power laws that used TSS + DOC + CHL as predictors were selected for further evaluation because these models were among the most skilled models within each form and using TSS-based models instead of NVSS + VSS-based models allowed us to maximize use of the cross-lake dataset since there were 93 more observations of TSS than VSS and NVSS. To evaluate the differential effect of VSS and NVSS on light attenuation prediction, we also included the multiple linear regression on NVSS + VSS + DOC + CHL in further analyses as a comparison to the TSS-based models we were evaluating. Skill metrics from the cross-validation and model fits for the four selected K_d-WQ regressions are shown in Table 1 and Fig. 4, respectively. Formulas for the linear regression on TSS + DOC + CHL (equation (8)), VSS + NVSS + DOC + CHL (equation (9)), power law (equation (10)), and segmented regression (equation (11)) models are reported below and in ESM Table S4 along with cross-validation skill metrics:

$$K_dPAR = 0.082(TSS) + 0.102(DOC) + 0.004(CHL) - 0.068 \tag{8}$$

$$K_dPAR = 0.033(VSS) + 0.09(NVSS) + 0.099(DOC) + 0.008(CHL) - 0.03 \tag{9}$$

$$K_dPAR = 0.178(TSS)^{0.511} * DOC^{0.439} * CHL^{0.058} * \varepsilon_{adj}, \varepsilon_{adj} = 1.06 \tag{10}$$

$$K_dPAR = \begin{cases} 0.092(TSS) + 0.097(DOC) + 0.004(CHL) - 0.084, TSS < 8.027 \\ 0.079(TSS) + 0.097(DOC) + 0.004(CHL) + 0.025, TSS \geq 8.027 \end{cases} \tag{11}$$

We calculated the relative contribution of each water quality variable to K_d(PAR) using the multivariate linear regressions listed as equations 8–9. Attenuation due to water was negative in both equations (8) and (9), which likely indicates a negligible contribution to K_d(PAR) and, therefore, we subtracted it from overall K_d(PAR) in the denominator to investigate the water quality drivers of K_d(PAR) and maintain their relative contributions ≤ 100%. In both equations (8) and (9), DOC was the primary factor affecting light attenuation in Lakes Michigan-Huron, Ontario, and the central and eastern basins of Lake Erie (Fig. 5). In equation (8), TSS was the main contributor to K_d(PAR) in western Lake Erie and Saginaw Bay. Disaggregating TSS into NVSS and VSS in equation (9) demonstrated that NVSS was more impactful on K_d(PAR) than VSS in western Lake Erie, but these constituents had relatively equal contributions in Saginaw Bay although NVSS' contribution was more variable in that basin. Regressions using VSS + NVSS in place of TSS appeared to have greater sensitivity to CHL; however, interpretation of this effect is limited owing to the fact that VSS + NVSS based regressions were based on a smaller sample size (610) than the TSS-based regressions (703). Most of the VSS + NVSS observations came from western Lake Erie and Saginaw Bay. DOC was also important in western

Table 1
Skill of four photosynthetically active radiation attenuation (K_d(PAR)) regressions on water quality (K_d-WQ regressions) when predicting on withheld data as determined via 10-fold cross-validation. Skill metrics are reported for two ranges of data: the entire dataset and at K_d(PAR) $< 0.3\ m^{-1}$. Other candidate K_d-WQ regressions' skill metrics are reported in ESM Table S4.

		Entire Dataset			K_d(PAR) $< 0.3\ m^{-1}$	
Predictors	Form	RMSE, m^{-1}	Adjusted r^2	n	RMSE, m^{-1}	n
TSS + DOC + CHL	Multivariate Regression	0.34	0.8	703	0.15	191
	Power law	0.37	0.82	703	0.16	191
	Segmented	0.35	0.83	703	0.15	191
NVSS + VSS + DOC + CHL	Multivariate Regression	0.34	0.85	610	0.13	126

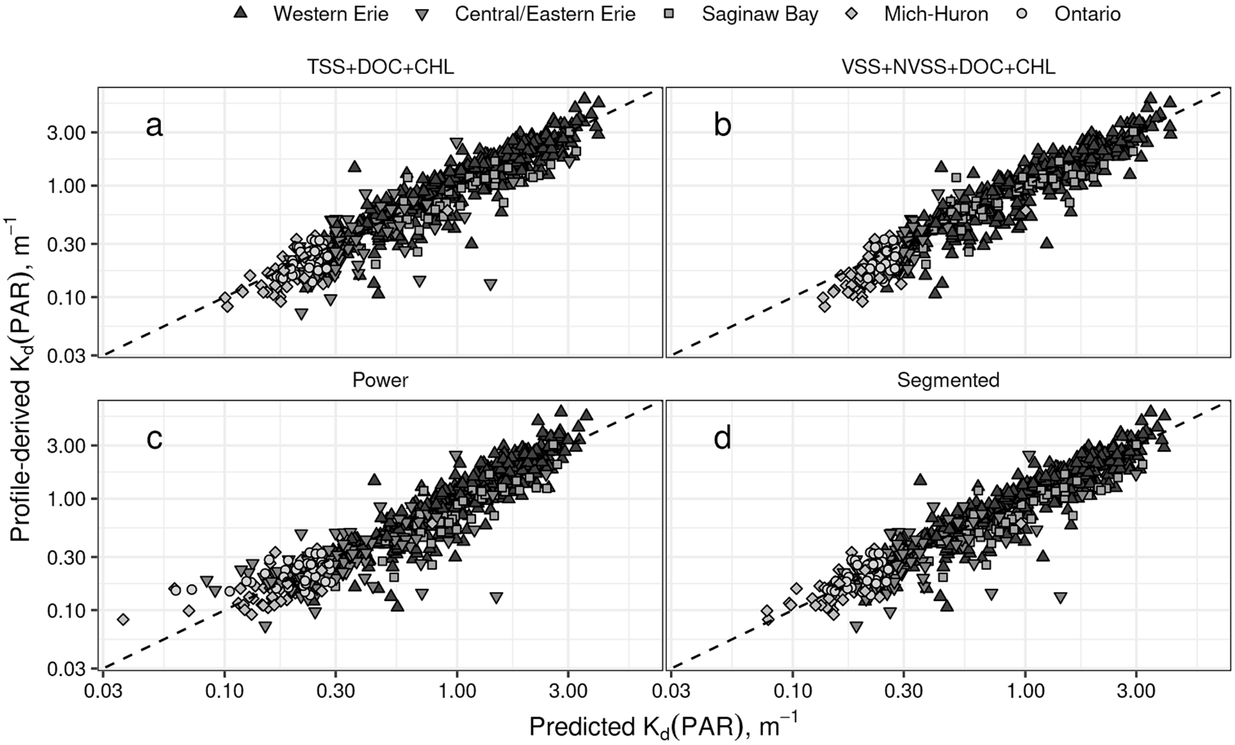

Fig. 4. Comparison of the attenuation coefficient for photosynthetically active radiation (K_d(PAR)) derived from PAR profiles from four Laurentian Great Lakes to K_d(PAR) predicted by four selected K_d(PAR)-Water Quality (K_d-WQ) regressions including: (a) a multivariate linear regression on total suspended solids (TSS, mg L^{-1}), dissolved organic carbon (DOC, mg L^{-1}), and chlorophyll-*a* (CHL, μg/L); (b) a multivariate linear regression on volatile suspended solids (VSS, mg L^{-1}), non-volatile suspended solids (NVSS, mg L^{-1}), DOC, and CHL; (c) a power law regression on TSS, DOC, and CHL; and (d) a segmented linear regression on TSS, DOC, and CHL. The dashed 1:1 line indicates perfect agreement between predictions and profile-derived values.

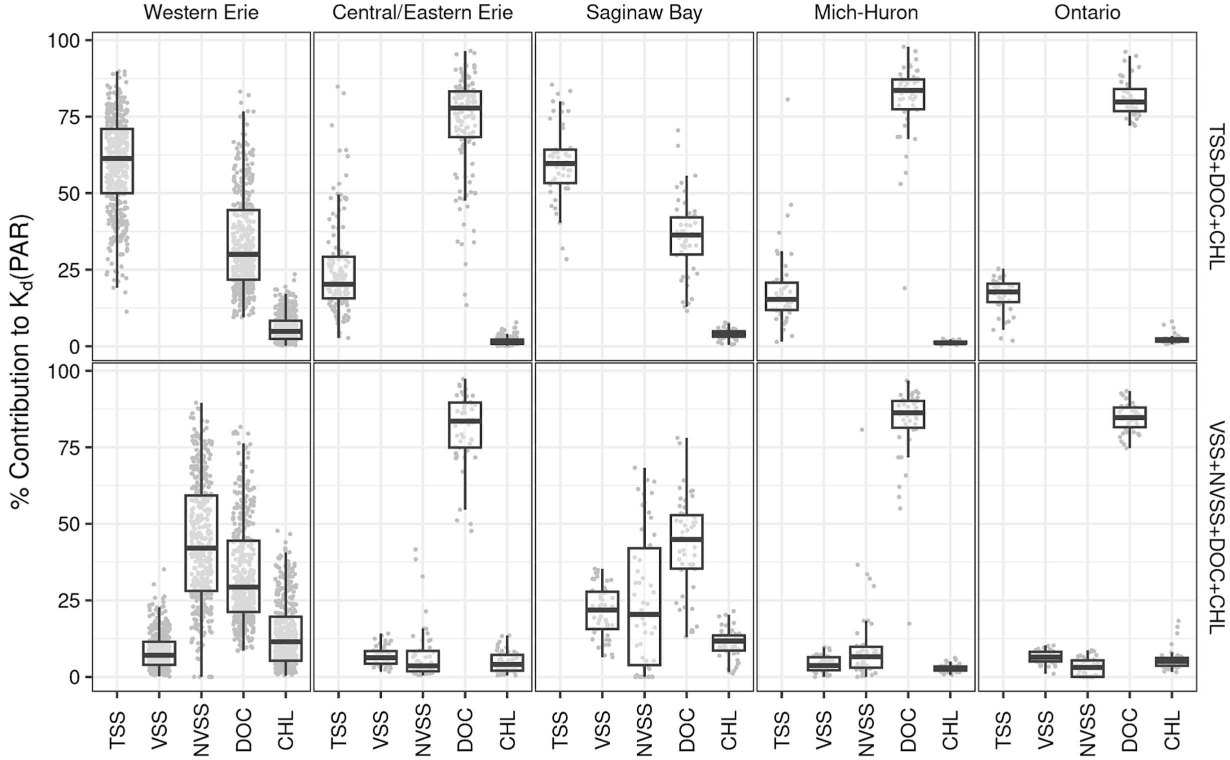

Fig. 5. Percent contribution of total suspended solids (TSS), non-volatile suspended solids (NVSS), volatile suspended solids (VSS), dissolved organic carbon (DOC), and chlorophyll-*a* (CHL) to the attenuation of photosynthetically active radiation (K_d(PAR)) for two different multivariate regressions (equations (8), (9), top row and bottom row, respectively). Percent contribution to K_d(PAR) was calculated by dividing the product of a given predictor's coefficient and corresponding concentration by the difference of the predicted K_d(PAR) and the intercept (equation (3)).

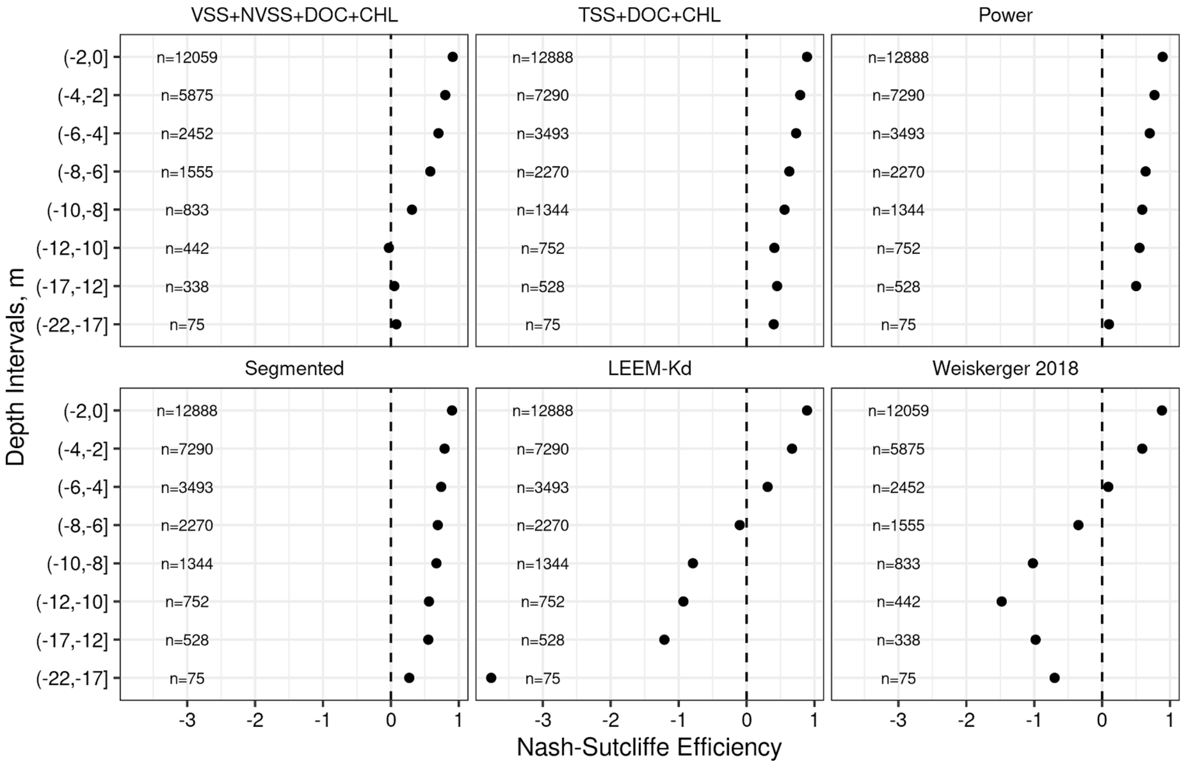

Fig. 6. Nash-Sutcliffe efficiency of six photosynthetically active radiation (PAR) models by depth interval using the attenuation coefficient of PAR (K_d(PAR)) predicted from different K_d(PAR)-Water quality (K_d-WQ) regressions. Simulated and observed PAR data comparisons were aggregated by depth intervals across profiles for this skill metric calculation. K_d-WQ regressions used in PAR models include two published regressions calibrated with western Lake Erie data (LEEM-Kd and Weiskerger 2018) and four regressions that were calibrated with our cross-lake dataset including: a multivariate linear regression on total suspended solids (TSS), dissolved organic carbon (DOC), and chlorophyll-*a* (CHL) ("TSS + DOC + CHL"); a multivariate regression on volatile suspended solids (VSS), non-volatile suspended solids (NVSS), DOC, and CHL ("VSS + NVSS + DOC + CHL"); a power law regression on TSS, DOC, and CHL ("Power"); and segmented regression on TSS, DOC, and CHL ("Segmented").

Table 2

Skill of the top two performing light attenuation-water quality regressions in simulating subsurface photosynthetically active radiation (PAR) profiles when implemented in equation (1) (i.e., PAR model) for each basin included in the cross-lake dataset. Model skill metrics were calculated for each individual profile and we report the median model skill of profiles ($n_{profile}$) by basin and across the whole dataset here. Skill metrics for all PAR models are reported in ESM Table S3..

Basin	K_d-WQ regression used in PAR model	relED (%)	NSE	$n_{profile}$
Western Erie	Segmented:TSS + DOC + CHL	16.63	0.83	422
	VSS + NVSS + DOC + CHL	17.61	0.81	420
Central & Eastern Erie	Power:TSS + DOC + CHL	13.83	0.92	227
	Segmented:TSS + DOC + CHL	15.90	0.89	227
Saginaw Bay	VSS + NVSS + DOC + CHL	13.98	0.89	45
	Weiskerger 2018	15.84	0.80	45
Mich-Huron	VSS + NVSS + DOC + CHL	15.86	0.87	32
	TSS + DOC + CHL	19.90	0.86	32
Ontario	VSS + NVSS + DOC + CHL	15.33	0.91	28
	Power:TSS + DOC + CHL	18.20	0.84	28
Whole dataset	Segmented:TSS + DOC + CHL	17.23	0.85	754
	VSS + NVSS + DOC + CHL	17.37	0.84	683

Lake Erie and Saginaw Bay. Median DOC contribution to K_d(PAR) in equation (8) for western Lake Erie and Saginaw Bay were 30% and 36.34%, respectively, and 29.3% and 44.89% in equation (9), respectively.

3.3. *Assessment of subsurface PAR prediction with observed water quality*

We estimated subsurface PAR (i.e. PAR model, e.g. ESM Figure S9) using equation (1) with I_0 estimated from the observed PAR profile and K_d(PAR) predicted from six K_d-WQ regressions. We used the four selected cross-lake K_d-WQ regressions (equations 8–11, Fig. 4) and the two published, western Lake Erie-trained K_d-WQ regressions (LEEM-Kd, Weiskerger et al., 2018) to predict K_d(PAR) from concurrent surface water quality measurements. The skill of each PAR model varied by depth and basin (Fig. 6 and ESM Figure S10, Tables 2 and ESM Table S5). All models evaluated demonstrated acceptable bias across depths in the western basin of Lake Erie (ESM Figure S10, Table S5). The four PAR models using cross-lake calibrated K_d-WQ regressions were more robust predictors of PAR across basins compared to those that used the LEEM-Kd and Weiskerger et al. (2018) regressions, but the most skilled PAR model differed by basin (Table 2). While most basins had several models that demonstrated similar median skill metrics in predicting subsurface PAR profiles, there was a larger gap in skill between PAR models assessed in Saginaw Bay. The best Saginaw Bay PAR model used the K_d-

Table 3
Suspended sediment (SS) model skill metrics assessed using two different types of *in-situ* data (SS_{obs}): non-volatile suspended solids (NVSS) from grab samples and NVSS converted from turbidity data.

Data type	Mean SS_{obs}, mg L^{-1}	σ_{obs}, mg L^{-1}	σ_{mod}, mg L^{-1}	Bias, mg L^{-1}	RMSE	r	NSE	n	Number of stations
Grab Sample	12.14	15.99	15.80	−0.21	13.76	0.62	0.25	125	8
Converted Turbidity	6.54	11.63	12.15	1.31	9.59	0.68	0.32	26,755	13

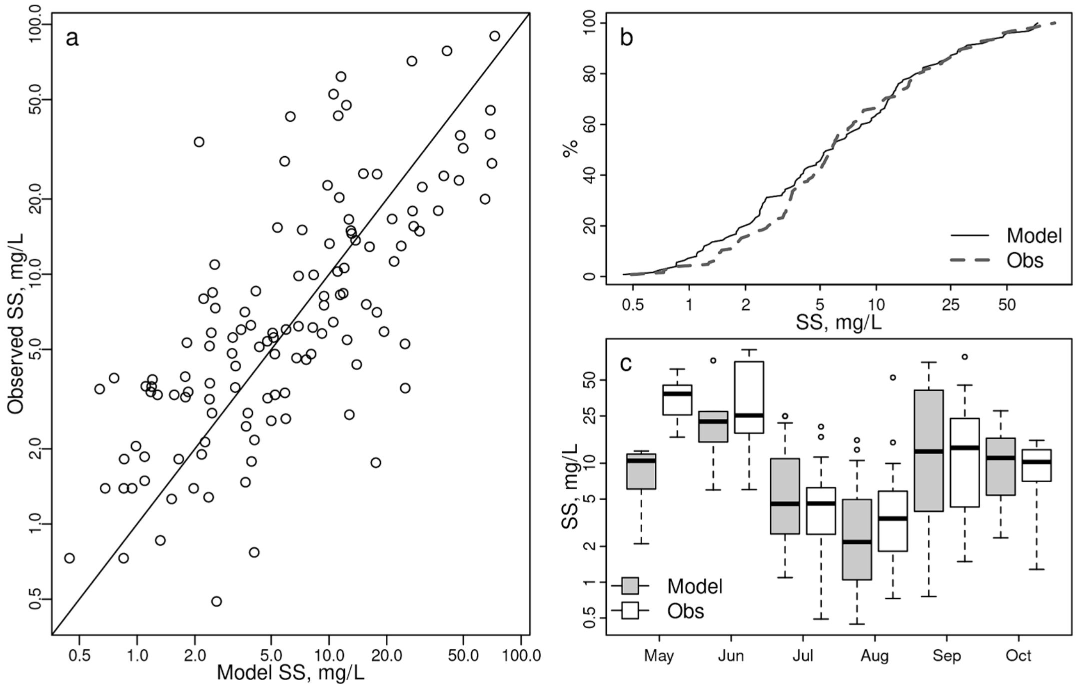

Fig. 7. a)Suspended sediment (SS) model-simulated surface SS vs *in-situ* grab samples of non-volatile suspended solids (NVSS) with a 1:1 line, b) cumulative distribution of simulated surface SS and *in-situ* grab samples of NVSS, and c) monthly distribution of simulated surface SS compared to corresponding *in-situ* grab samples of NVSS. Simulated NVSS ranged from 0.44-72.94 mg/L and observed NVSS ranged from 0.49 – 89.87 mg/L.

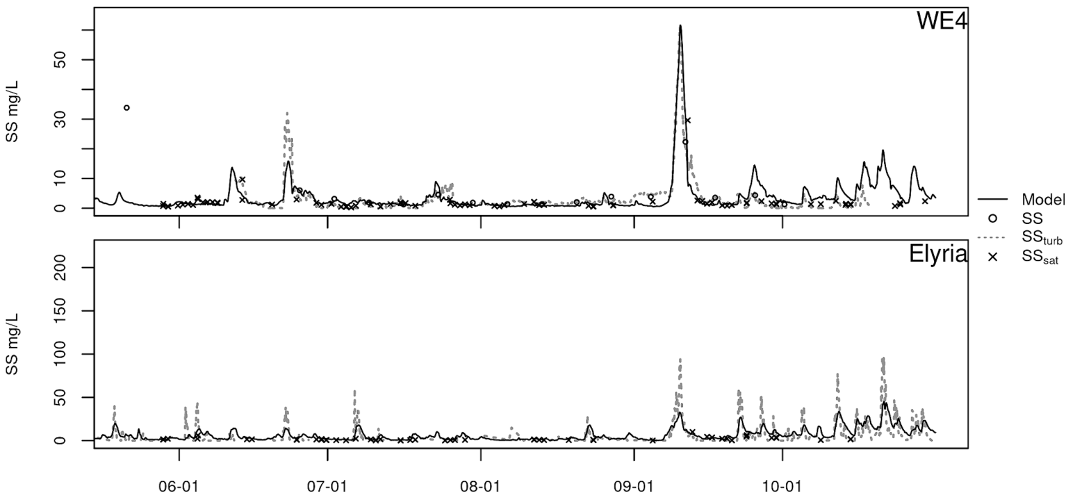

Fig. 8. Suspended sediment (SS) model predicted surface SS (solid line) at the western basin site WE4 and the central basin site Elyria compared to non-volatile suspended solids (NVSS, circles) from grab samples, estimated from turbidity sensor data ($SS_{turb,}$ dashed line), and from bias-corrected satellite data (SS_{sat}, X's).

WQ regression on VSS + NVSS + DOC + CHL followed by the Weiskerger et al. (2018) regression, but the next best model's relED was 11.5% lower and produced a NSE that was 0.13 lower. Model skill tended to deteriorate with depth, as error in prediction of light transmission is cumulative over depth. Three of the four models calibrated with the cross-lake dataset maintained an NSE > 0 at all depth intervals (Fig. 6). The PAR model using the regression on VSS + NVSS + DOC + CHL at 10–12 m was the only instance where a model using a cross-lake K_d-WQ regression produced a negative NSE (−0.03). Error in subsurface PAR predicted by the Weiskerger et al. (2018) and LEEM-Kd PAR models exceeded observed variance in PAR (i.e., NSE < 0) between 6 and 22 m.

3.4. Lake Erie case study: FVCOM-SS-DOC model evaluation

Prior to using the cross-lake calibrated K_d-WQ regressions in the Lake Erie FVCOM-SS-DOC model, we calibrated the SS model and compared simulated DOC against observations. Calibration and evaluation of FVCOM-SS-DOC is reported below.

We calibrated the two erodibility parameters (M, τ_{CR}) based on data summarized by the Great Lakes Aquatic Habitat Framework (GLAHF) (Riseng et al., 2018), site-specific comparisons to observations, and spatial comparisons to satellite data. Calibration of the bed sediments resulted in five sediment types distinguished by their combination of M and τ_{CR} (Fig. 1b). A majority of the sediment bed was classified under two of the five sediment types including western basin mud ($M = 1.25\cdot10^{-6}$ kg m^{-2} s^{-1}, $\tau_{CR} = 0.15$ Pa) and central and eastern basin mud ($M = 2.5\cdot10^{-7}$, $\tau_{CR} = 0.15$ Pa). Regions of the model identified as hard/rock in the GLAHF data layer were set to be non-erodible ($M = 0$ kg m^{-2} s^{-1}, $\tau_{CR} = 8.25$ Pa). The other two sediment types were implemented over smaller areas to refine the SS model's ability to simulate spatial patterns apparent in satellite imagery. More information on the regional bed parameterization can be found in the ESM.

The SS model compared well against *in-situ* data. Compared to NVSS grab samples, which were predominantly collected in the western basin, the model predicted SS concentrations with minimal bias across the entire range of observations (Table 3, Fig. 7a,b). The model was biased low in May and underestimated the observed variance in June 2018, but compared better to observations from July – October (Fig. 7c). All 13 stations had some turbidity data, and the model demonstrated apt skill compared against this dataset set as well (Table 3).

We assessed simulated SS using observed time-series of SS derived from turbidity sensor data, NVSS from grab samples, and bias-corrected satellite-derived SS (Fig. 8, ESM Figs. S11–S21). Model skill varied by station (ESM Table S6), with the best performance at the western basin sites, particularly WE4 and WE2 (Fig. 8 and ESM Fig. S11). At WE4, simulated SS was highly correlated to sensor observations ($r = 0.86$), bias was low (Bias = 0.4 mg L^{-1}, RMSE = 3.33 mg L^{-1}), and the model captured the variability of the observations well (NSE = 0.71, $\sigma_{obs} = 6.17$ mg L^{-1}, $\sigma_{mod} = 6.32$ mg L^{-1}) (Fig. 8). Resuspension events in late June, late July, and a large event in early September indicated in the sensor observations were all simulated by the model. Simulated SS compared well to the large resuspension event in September, considering the onset, rate of increase in surface SS, peak concentration, and rate of decline. Simulated SS also compared well to observations at WE2, which had turbidity data from May – October (Bias = -1.4 mg L^{-1}, RMSE = 11.54 mg L^{-1}, NSE = 0.51, $\sigma_{obs} = 16.57$ mg L^{-1}, $\sigma_{mod} = 12.21$ mg L^{-1}) (ESM Figure S11). Simulated SS underestimated peak concentrations in large resuspension events at WE2, including one in late May and early September, but the timing and rate of change in surface SS was well simulated for most resuspension events aside from the late May event.

In the central basin, the SS model was less skilled in predicting site-specific time-series of SS relative to its performance in the western basin (ESM Table S6), but it still captured nearshore-offshore differences and simulated most resuspension events when they occurred (Fig. 8 and Figures S20-S21). Simulated SS underestimated peak concentrations at all central basin sites. The SS model simulated the lower levels of SS observed at the two offshore central basin stations, CHRP2 (ESM Figure S20) and CHRP9 (Figure S21), compared to the more nearshore site near Elyria, OH (Fig. 8). The SS model also underestimated converted turbidity data at the two offshore stations in the central basin during periods of resuspension (ESM Figures S20-S21). However, there was disagreement between the bias-corrected satellite data and the converted turbidity data at times and the SS model tended to show stronger agreement with the satellite data.

The SS model simulated common spatial patterns of SS and episodic resuspension events observed in VIIRs imagery (Fig. 9 and ESM Fig. S22). Compared to satellite data across the whole lake, the SS model was able to predict SS concentrations with low bias and positive NSE, although skill metrics varied by basin (Table 4). Common spatial patterns of SS in the satellite imagery that were simulated included a persistent difference in SS concentrations in the northern half of the western basin compared to the southern half (Fig. 9a-f), a SS plume extending from the western basin's eastern limit to Sandusky, OH (Fig. 9a-b,e-f), and elevated SS along the central basin's northern shoreline (Fig. 9a-f), which varied in extent and concentration. The SS model also simulated spatial patterns associated with a large resuspension event that was detected by all three types of observations in early September 2018 (ESM Figures S11-S22). The model's performance during this event is described further in the ESM.

We evaluated DOC simulated by FVCOM-SS-DOC using 270 observations from three sampling programs in Lake Erie. FVCOM-SS-DOC overestimated average observed DOC by 0.15 mg L^{-1} throughout the lake and had an RMSE of 0.49 mg L^{-1}. Simulated DOC in the central and eastern basins agreed well with observations but was biased high in the western basin and underestimated observed variability (ESM Figure S23). The observations indicated lower DOC in the western basin compared to the other two basins, which was not simulated by FVCOM-SS-DOC.

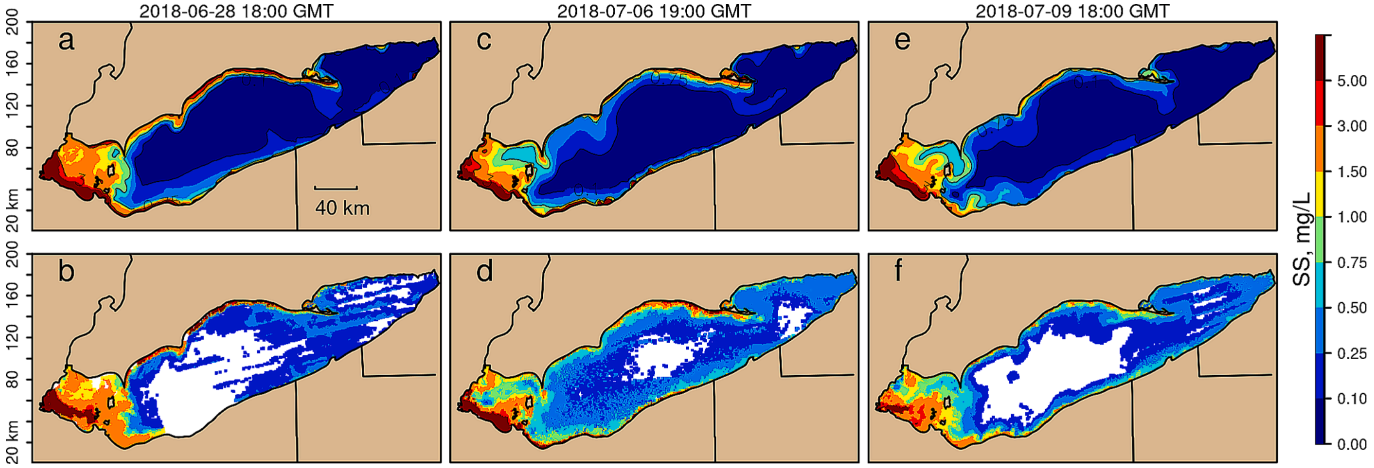

Fig. 9. Comparison of common spatial patterns of surface suspended sediments (SS) simulated by the Finite Volume Community Ocean Model's Suspended Sediment model (FVCOM-SS; a,c,e) to satellite-derived estimates from the color-producing agent algorithm (b,d,f) as represented in three examples from June 28, July 6th, and July 9th 2018.

Table 4

Suspended sediment (SS) model skill in comparison to bias-corrected satellite suspended mineral data (SS_{sat}) across Lake Erie and it's three basins. Satellite data spanned from 2018 to 05-28 to 2018–9-29.

Basin	Mean SS_{sat}, mg L^{-1}	Bias, mg L^{-1}	RMSE, mg L^{-1}	r	NSE	σ_{sat}, mg L^{-1}	σ_{mod}, mg L^{-1}	n
Western	3.04	0.85	4.75	0.65	0.08	4.96	6.00	85,805
Central	0.77	−0.21	1.5	0.55	0.19	1.66	1.42	155,437
Eastern	0.41	−0.2	0.51	0.42	−0.4	0.44	0.45	62,498
Lake wide	1.34	0.09	2.75	0.68	0.21	3.09	3.7	303,740

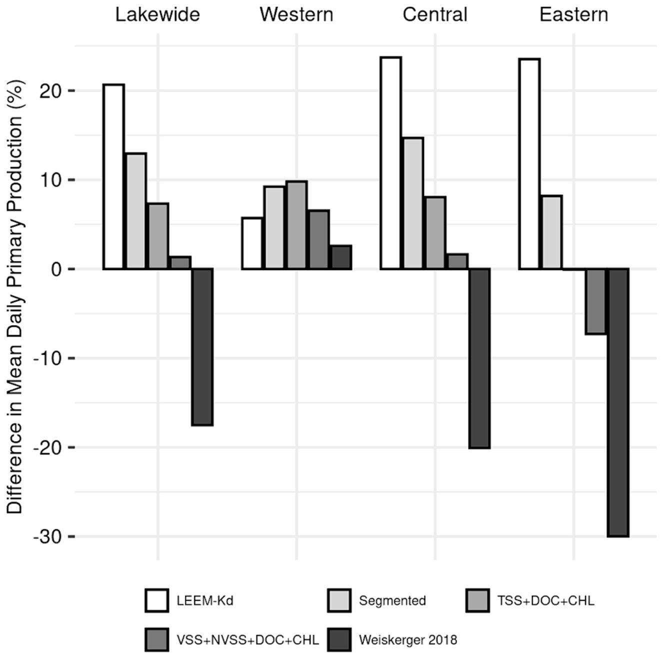

Fig. 10. Sensitivity of lake wide and basin-specific estimated daily primary production (PP) from April 1st – September 30th, 2018 using the Great Lakes primary production model (Fahnenstiel et al., 1989; Fahnenstiel et al., 2016; Lang and Fahnenstiel, 1996) and the attenuation coefficient of photosynthetically active radiation (K_d(PAR)) predicted by four cross-lake calibrated K_d(PAR)-water quality (K_d-WQ) regressions and two western basin calibrated K_d-WQ regressions (LEEM-Kd and Weiskerger 2018). Water quality and suspended sediment data simulated by the Finite Volume Community Ocean Model's Suspended Sediment and Dissolved Organic Carbon Model (FVCOM-SS-DOC) were used as inputs to the primary production model. All primary production estimates were reported as the percent difference relative to the primary production prediction from the cross-lake calibrated power law regression on total suspended solids (TSS), DOC, and chlorophyll.

3.5. *Lake Erie case study: Assessment of K_d(PAR) and primary production prediction with simulated water quality from FVCOM-SS-DOC*

We used the four selected cross-lake K_d-WQ regressions (equations 8–11, Fig. 4) and the two published, western Lake Erie-trained K_d-WQ regressions (LEEM-Kd, Weiskerger et al., 2018) to predict K_d(PAR) from water quality data simulated by FVCOM-SS-DOC. We also assessed the sensitivity of lake-wide mean estimates of daily primary production rates to selection of K_d-WQ regression used with FVCOM-SS-DOC. All models produced positive NSE values in simulating K_d(PAR) when given simulated water quality and SS concentrations (ESM Figure S24). The power law on TSS + DOC + CHL produced the best fit to profile-derived K_d(PAR) values. The simulated water quality fields we prescribed for this analysis limited the skill of K_d-WQ regressions in the central basin. The lack of variation in the CHL and VSS fields prevented K_d-WQ regressions from being able to predict variation in K_d(PAR) below 0.25 m^{-1}, which was characteristic of some central basin profiles used in this assessment.

The sensitivity of primary production to K_d-WQ regression was evaluated as the percent difference relative to the primary production prediction from the power law regression on TSS + DOC + CHL (Fig. 10). All cross-lake calibrated K_d-WQ regressions were able to predict K_d(PAR) across the optical gradient in the LGL, but the power law regression was chosen as the baseline model because it was among the best performing in Lake Erie when given observed or simulated inputs (Tables 2 and ESM S5, Figure S24). Weiskerger et al. (2018) produced the lowest lake wide primary production estimates that were 17.5% lower than the cross-lake calibrated power law, whereas LEEM-Kd produced the highest relative estimate (Percent difference = 20.67). The other cross-lake calibrated regressions differed from the power law's predicted primary production by 1.3–12.9%. Percent difference in primary production estimates in the central and eastern basins followed the ranking described for the lake wide estimates with LEEM-Kd and Weiskerger et al. (2018) being ≥ 20% different than primary production derived from the power law. Primary production estimates in western basin were comparable amongst all K_d-WQ regressions (2.5–9.8% different than power law).

3.6. *Lake Erie case study: Assessment of simulated spatial patterns of Lake Erie K_d(PAR) against satellite estimates*

We implemented the power law regression on TSS + DOC + CHL in the 3D Lake Erie FVCOM-SS-DOC code and assessed simulated K_d(PAR) against satellite-derived K_d(PAR) estimates in 2018. We found that satellite-derived K_d(PAR) agreed well with corresponding estimates from subsurface PAR profiles ($r^2 = 0.93$; ESM Figure S25), supporting their use in model skill assessment. FVCOM-SS-DOC simulated K_d(PAR) with low bias across the entire lake and produced positive NSE values (Table 5). The model's ability to simulate variability in K_d(PAR) decreased from west to east, which was also reflected in model skill metrics. The model simulated recurrent and episodic spatial patterns indicated in the satellite imagery that reflected the dynamics of the SS model. This includes the north–south difference in the western basin, increased K_d(PAR) along the north shore of the central basin, and higher

Table 5

Skill assessment comparing the attenuation of photosynthetically active radiation (K_d(PAR)) simulated by a power law on total suspended solids (TSS), dissolved organic carbon (DOC), and chlorophyll-*a* (CHL) implemented in the Finite Volume Community Ocean Model's Suspended Sediment and Dissolved Organic Carbon model (FVCOM-SS-DOC, a,c,e) and corresponding satellite-derived estimates of K_d(PAR) (b,d,f). Satellite data spanned from 2018 to 05-28 to 2018–9-29.

Basin	Mean $K_d(PAR)_{sat}$, m^{-1}	Bias, m^{-1}	RMSE, m^{-1}	r	NSE	σ_{sat}, m^{-1}	σ_{mod}, m^{-1}	n
Western	0.84	0.00	0.32	0.79	0.61	0.52	0.46	66,434
Central	0.36	−0.04	0.21	0.67	0.41	0.28	0.15	151,234
Eastern	0.26	−0.04	0.2	0.36	0.09	0.21	0.09	68,679
Lakewide	0.45	−0.03	0.24	0.81	0.64	0.40	0.34	286,347

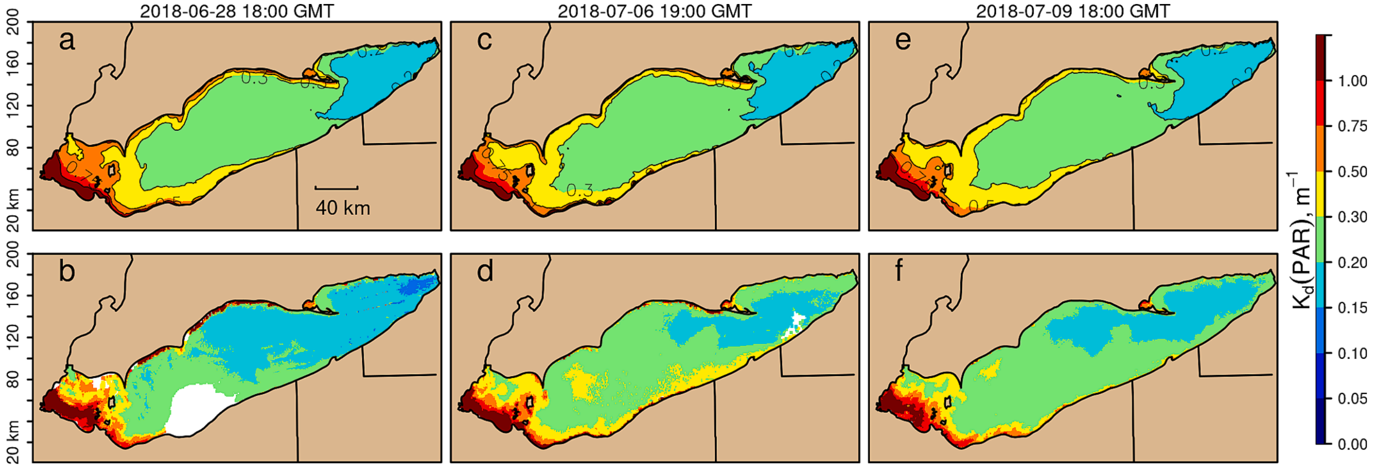

Fig. 11. Comparison of the attenuation of photosynthetically active radiation (K_d(PAR)) simulated by a power law on total suspended solids (TSS), dissolved organic carbon (DOC), and chlorophyll-*a* (CHL) implemented in the Finite Volume Community Ocean Model's Suspended Sediment and Dissolved Organic Carbon Model (FVCOM-SS-DOC; a,c,e) to corresponding satellite-derived estimates of K_d(PAR) (b,d,f) for three dates in late June and early July.

attenuation along the sediment plume that occasionally extends from the western basin into the Sandusky subbasin (Fig. 11). The model also simulated a gradient of decreasing attenuation from west to east and from nearshore to offshore that was indicated in the satellite data (Fig. 11).

4. Discussion

Previously published implementations of K_d-WQ regressions have been calibrated over a range of K_d(PAR) values that limits their performance in other parts of the LGL with different levels of water transparency thereby limiting their utility to biophysical models (Higgins et al., 2005; Limnotech, 2021; Rowe et al., 2017; Weiskerger et al., 2018). In comparison to Weiskerger et al. (2018) and LEEM-Kd, the four cross-lake calibrated regressions we evaluated were more skilled in predicting K_d(PAR) and PAR in transparent waters with euphotic zones deeper than 6 m. Moreover, the increased flexibility of the cross-lake calibrated regressions did not reduce K_d(PAR) and PAR simulation skill in the western basin relative to the western basin trained regressions. Having K_d-WQ regressions that can work across the water transparency gradient within a given LGL is important to simulating higher order ecosystem processes, such as primary production, which we demonstrated by using the six evaluated K_d-WQ regressions with simulated data from our simplified Lake Erie biophysical model, FVCOM-SS-DOC. Furthermore, we were able to verify that FVCOM-SS-DOC could simulate spatial patterns in SS and K_d(PAR) observed in Lake Erie when implemented with one of our top-performing cross-lake K_d-WQ regressions thereby highlighting how our calibration of 25 K_d-WQ regressions can advance the development of biophysical models needed to support ecosystem management objectives in the LGL.

4.1. The variable light environment in the Laurentian Great Lakes

Variability in K_d(PAR) within and across the LGL is substantial when considered in context of what has been observed in marine and freshwater environments. We documented K_d(PAR) ranges from 0.072-6.2 m^{-1} with coefficients of variation ranging between 30–78% by basin and 90% across the entire dataset. Morris et al. (1995) found K_d(PAR) in 59 inland lakes across the northeastern United States, Alaska, Colorado, and Argentina ranged from 0.1-5.73 m^{-1} with a coefficient of variation of 8.7%. Song et al. (2017) used an empirical relationship of Landsat reflectance to estimate K_d(PAR) for 178 lakes in northeast China, which ranged from 0.49 m^{-1} to 15.8 m^{-1}, although only four measurements in their calibration dataset ($n = 167$) exceeded 8 m^{-1}. The LGL's range in K_d(PAR) indicated in our dataset is comparable to what has been observed in in the Atlantic Ocean and is only slightly narrower than what has been measured in open water and coastal environments across the world's major oceans and seas when pooled together (range: 0.03–9.85 m^{-1}; Son and Wang, 2015). The variability of light attenuation in the LGL underscores the importance of fitting K_d-WQ regressions to a dataset that adequately represents the range of optical conditions across the lakes.

4.2. K_d(PAR) partitioning using K_d-WQ regressions

There was a dichotomy that emerged in the partitioning of K_d(PAR) in each basin based on coefficients from equations (8) and (9). 75–83% of K_d(PAR) on average was due to DOC and 16–25% was due to TSS in the basins that mostly comprised of open water samples (Mich-Huron, Central/Eastern Erie, Ontario). In the most opaque basins (Lake Erie's western basin and Saginaw Bay), TSS and DOC accounted for about 60% and 35% of K_d(PAR), respectively. The contribution of DOM to K_d(PAR) relative to suspended particulates in the LGL, even in western Lake Erie and Saginaw bay, are notably higher than what has been reported in other systems where this has been evaluated including the eutrophic Lakes Taihu (% Contribution of CDOM to K_d(PAR) = 6.8%, Zhang et al., 2007) and Donghu in China (17.8–23.9%, Yang et al., 2005), the oligotrophic Dom Helvécio lake in Brazil (4.8%, Brandao et al., 2017), Arhus Bay of the Kattegat between the North and Baltic seas (17%, Lund-Hansen, 2004), the Indian River Lagoon in Florida (5–25%, Christian and Sheng, 2003), and Japan's eastern Seto Inland Sea (13%, Yamaguchi et al., 2013). The contribution of CDOM to K_d(PAR) reported by Chen et al. (2014) for the Caloosahatchee River Estuary in Florida demonstrated contributions of CDOM (range: <5–90%, mean contribution: 55%) within the range of average contributions of DOC by basin in the LGL (35–83%). It should be noted that our percent contribution refers to the percent contribution of DOC to light attenuation of non-water components since our estimated K_w was negative, whereas these other studies calculated contributions of CDOM based on regressions with a forced, positive constant for K_w (0.027–0.15 m^{-1}) that accounted for an additional 0.2–10% of K_d(PAR) depending on the system. Choosing a forced or fitted intercept likely would not affect conclusions regarding the relative importance of each constituent to overall light attenuation since the attenuation due to water is often lower than attenuation due to the non-water components (Chen et al., 2014).

Our findings are consistent with relative contribution of dissolved and particulate components to IOPs in the LGL documented in previous studies. Perkins et al. (2013) found CDOM and total particulates (algae and non-algae) contributed, on average, 39% and 61% to total absorption of the 440 nm wavelength, respectively, in Lake Erie's western basin, Green Bay, and Sandusky Bay, and 57% and 40%, respectively, in open waters of Lakes Superior, Michigan, Huron, Ontario, and Lake Erie's central and eastern basins. Effler et al. (2013) found that minerogenic particles accounted for 80% of backscattering in the western basin and Sandusky Bay but were less influential on backscattering in most open water locations. While the contributions to K_d(PAR) cannot be equated to the contributions to IOPs since the influence of absorption and backscattering on total attenuation are not equal (Lee et al., 2005), our study reinforces the relative importance of dissolved organic matter in offshore waters and total particulate matter in coastal waters as determining factors of the underwater light field in the LGL.

4.3. Lake Erie case study

The calibration of the SS model in FVCOM-SS-DOC was a prerequisite to modeling light attenuation in Lake Erie because SS is a major driver of light attenuation (Weiskerger et al., 2018). The SS model simulated the recurrent patterns of resuspension seen along the south shore of the western basin and the north shore of the central basin. It also simulated episodic events like that observed in September 2018. By using three different datasets to calibrate our SS model, we were able to do an extensive quantitative comparison of our model to site-specific *in-situ* data and bias-corrected satellite data. Previous studies have used converted beam attenuation (Hawley et al., 2014), backscatter and turbidity data (Khazaei et al., 2021; Lin et al., 2021), and satellite true color imagery (Limnotech, 2021; Niu et al., 2018) to supplement intermittent grab sample data for quantitatively and qualitatively evaluating SS models. Our calibration approach is similar to that employed by Khazaei et al. (2021) for their sediment transport model of Green Bay, Lake Michigan and represents an improvement on previous calibration efforts in Lake Erie SS models by expanding the number of observations for quantitative model evaluation. As a result, our SS model demonstrated skill (Tables 3 and 4) that was comparable or better than other published SS models in the LGL including LEEM ($r^2 = 0.2$, Bias = -2.2 mg L^{-1} of TSS; Limnotech, 2021), Niu et al. (2018)'s western Lake Erie SS model ($r^2 = -0.07 – 0.78$, RMSE = 5.1–28.2 mg L^{-1} of TSS), Lin et al. (2018)'s Lake Erie sediment transport model (near bed turbidity: $r^2 = 0.39$), and Khazaei et al. (2021)'s Green Bay, Lake Michigan sediment transport model (Grab samples: Bias = -6.57–1.38 mg L^{-1} of TSS, r = 0.48–0.85). It should be noted that these aforementioned SS models simulate TSS, which includes inorganic and organic material, whereas we are simulating only the inorganic component.

Simulated DOC and SS concentrations from FVCOM-SS-DOC were sufficiently accurate to characterize general spatial patterns in K_d(PAR) when used with the cross-lake calibrated K_d-WQ regressions, but our case study shows the challenge of modeling variation in K_d(PAR) in more transparent waters for which SS is not the main driver. While it was well suited to simulate K_d(PAR) in the turbid, western basin of Lake Erie, FVCOM-SS-DOC was limited in its ability to predict variation in K_d(PAR) in the more transparent central and eastern basins, even though our K_d-WQ regressions showed improved performance at low K_d(PAR) compared to the previously published K_d-WQ regressions. The lack of dynamic particulate organic matter (CHL and VSS) in our biophysical model and the model's limited design in regards to DOC sources and sinks likely constrained FVCOM-SS-DOC's skill in areas of the lake where NVSS was not the primary driver of light attenuation. Such is the case for the central and eastern basins of Lake Erie, where DOC accounted for 75% of K_d(PAR) (Fig. 5) and VSS comprised 76% of TSS on average, compared to in the western basin where it comprised only 35%. The increased relative influence of organic matter on attenuation in more transparent waters highlights the tighter coupling of phytoplankton, phytoplankton-derivatives (e.g. POM, DOM), and light in offshore waters of the LGL relative to turbid coastal areas. Our calibrated K_d-WQ regressions can be incorporated into various biophysical model configurations, and may be expected to accurately predict K_d(PAR) if optically active constituents are accurately simulated.

4.4. Ecological implications

Model-predicted primary production for Lake Erie was sensitive to selection of K_d-WQ regression. All model primary production estimates for the western basin in 2018 were in relatively close agreement with each other (Fig. 10), but there was notable difference amongst the western basin calibrated and cross-lake calibrated regressions in the other two basins. Despite being both trained on western basin data, the LEEM-Kd and Weiskerger et al. (2018) regressions generated the most divergent primary production estimates of the six regressions evaluated in all basins except the western, and they respectively overestimated and underestimated all cross-lake calibrated regressions' lake wide primary production estimates. In the central and eastern basins, the LEEM-Kd and Weiskerger et al. (2018) regressions resulted in primary production estimates that were -30–20% different than estimates from the cross-lake calibrated power law regression on TSS + DOC + CHL (Fig. 10). Conversely, primary production estimated from the cross-lake calibrated regressions tended to agree with each other—with an average percent difference relative to the power law of 5.2% and 8.1% in the central and eastern basins, respectively. The divergence of LEEM-Kd and Weiskerger et al. (2018) in the central and eastern basins demonstrates the uncertainty associated with extrapolating K_d-WQ regressions trained on basin-specific data across the wide-ranging gradient of water transparency that exists within Lake Erie and the other LGL. In ecological models, biases in primary production caused by biases in subsurface PAR may affect model predictions of hypoxia (e.g., Moriarty et al., 2021), phytoplankton dynamics, and other processes indirectly or directly influenced by light.

Biophysical models with skillfully-resolved light environments can be vital tools for disentangling the role of light and other factors affecting harmful algal blooms (HABs), hypoxia, nuisance algae, and fisheries in the LGL. In Lake Erie, predicting the extent, transport, and toxicity of the bloom-forming cyanobacterium, *Microcystis aeruginosa*, has been a primary focus for biophysical model development informed by Annex 4 of the Great Lakes Water Quality Agreement (Annex 4 Objectives and Targets Task Team, 2015; Wynne et al., 2011). Differences in absorbance spectra and the ability to access light via buoyancy can confer a circumstantial competitive advantage to *Microcystis* (Huisman et al., 2004; Tan et al., 2020), but the concurrent effects of other factors, like nutrients and turbulence, obscure the role each driver plays in affecting seasonal succession of phytoplankton (Huisman et al., 2004; Liu et al., 2021). Additionally, predicting central basin hypoxia and eastern basin blooms of the filamentous green algae *Cladophora glomerata* in Lake Erie and their response to nutrient load management have been priority objectives guiding the development of biophysical models for the lake (Annex 4 Objectives and Targets Task Team, 2015; Limnotech, 2021). Subsurface PAR regulates *Cladophora* growth potential and is highly correlated with maximum sustainable biomass, which when exceeded can lead to sloughing of biomass that may ultimately contaminate beaches (Auer et al., 2010; Higgins et al., 2005). In regards to hypoxia, PAR can influence benthic dissolved oxygen by regulating oxygen production from benthic photosynthesis (Brothers et al., 2014; Brothers et al., 2017) and by affecting the growth of algae that ultimately settles out and consumes hypolimnetic oxygen through decomposition (Carrick et al., 2005; Lashaway and Carrick, 2010).

5. Conclusion

By consolidating a large database of coincident PAR and water quality observations across four of the five LGL, we were able to develop improved K_d-WQ regressions across a range of optical conditions observed in this system. We provide in the ESM the cross-lake dataset used for calibration and these calibrated regressions, which may be applied in biophysical models configured with a variety of state variables. We demonstrated how these models perform in predicting subsurface PAR when given incident PAR and concurrent water quality measurements as well as how they perform when given water quality concentrations simulated by a simplified biophysical model of Lake Erie. The former demonstrates the overall skill of several K_d-WQ regressions when provided accurate inputs and the latter demonstrates how the K_d-WQ regressions can be applied in a biophysical model to simulate spatial and temporal patterns of K_d(PAR). These advancements are important for future development of other ecological processes in LGL biophysical models that are influenced by light. Accurately resolving light attenuation for biophysical and biogeochemical models is a fundamental development step in order to use these tools to study the ecology of coastal and open waters in the LGL.

CRediT authorship contribution statement

Peter J. Alsip: Conceptualization, Data curation, Formal analysis, Investigation, Methodology, Software, Validation, Visualization, Writing – original draft, Writing – review & editing. **Mark D. Rowe:** Conceptualization, Data curation, Funding acquisition, Methodology, Project administration, Resources, Software, Supervision, Writing – review & editing. **Alexander Kain:** Data curation, Investigation, Methodology, Software, Validation, Writing – review & editing. **Casey Godwin:** Conceptualization, Data curation, Funding acquisition, Methodology, Project administration, Supervision, Writing – review & editing.

Declaration of competing interest

The authors declare that they have no known competing financial interests or personal relationships that could have appeared to influence the work reported in this paper.

Acknowledgements

We would like to thank Dr. Jianzhong Ge for sharing files that helped us set up the suspended sediment model. We also would like to thank Drs. Tom Hollenhorst, James Pauer, Megan McCusker, Jeff May, Craig Stow, and Paul Glyshaw for sharing PAR and water quality used in our database. We thank the reviewers of this manuscript for their time, effort, and thoughtful critiques. Funding was awarded to the Cooperative Institute for Great Lakes Research (CIGLR) through the NOAA Cooperative Agreement with the University of Michigan (NA17OAR4320152, NA22OAR4320150) and NOAA's National Centers for Coastal Ocean Science Competitive Research Program under Grant NA16NOS4780209 to the University of Michigan. This is CHRP contribution 267. This is GLERL contribution 2046 and CIGLR contribution 1240.

Appendix A. Supplementary data

Supplementary data to this article can be found online at https://doi.org/10.1016/j.jglr.2024.102364.

References

Abdelrhman, M.A., 2017. Quantifying contributions to light attenuation in estuaries and coastal embayments: application to Narragansett Bay, Rhode Island. Estuaries Coast 40, 994–1012.

Anderson, E., Fujisaki-Manome, A., Kessler, J., Lang, G., Chu, P., Kelley, J., Chen, Y., Wang, J., 2018. Ice forecasting in the next-generation great lakes operational forecast system (GLOFS). Journal of Marine Science and Engineering 6.

Annex 4 Objectives and Targets Task Team, 2015. Final report to the nutrients annex subcommittee: recommended phosphorus loading targets for lake Erie. Retrieved 05/24/2023. https://www.epa.gov/glwqa/report-recommended-phosphorus-loading-targets-lake-erie.

Auer, M.T., Tomlinson, L.M., Higgins, S.N., Malkin, S.Y., Howell, E.T., Bootsma, H.A., 2010. Great Lakes Cladophora in the 21st century: same algae—different ecosystem. J. Great Lakes Res. 36, 248–255.

Beletsky, D., Schwab, D.J., Roebber, P.J., McCormick, M.J., Miller, G.S., Saylor, J.H., 2003. Modeling wind-driven circulation during the March 1998 sediment resuspension event in Lake Michigan. J. Geophys. Res. Oceans 108.

Bocaniov, S.A., Leon, L.F., Rao, Y.R., Schwab, D.J., Scavia, D., 2016. Simulating the effect of nutrient reduction on hypoxia in a large lake (Lake Erie, USA-Canada) with a three-dimensional lake model. J. Great Lakes Res. 42, 1228–1240.

Boegehold, A.G., Burtner, A.M., Camilleri, A.C., Carter, G., DenUyl, P., Fanslow, D., Fyffe Semenyuk, D., Godwin, C.M., Gossiaux, D., Johengen, T.H., Kelchner, H., Kitchens, C., Mason, L.A., McCabe, K., Palladino, D., Stuart, D., Vanderploeg, H., Errera, R., 2023. Routine monitoring of western Lake Erie to track water quality changes associated with cyanobacterial harmful algal blooms. Earth Syst. Sci. Data 15, 3853–3868.

Bramm, M.E., Lassen, M.K., Liboriussen, L., Richardson, K., Ventura, M., Jeppesen, E., 2009. The role of light for fish-zooplankton-phytoplankton interactions during winter in shallow lakes - a climate change perspective. Freshw. Biol. 54, 1093–1109.

Brandao, L.P.M., Brighenti, L.S., Staehr, P.A., Barbosa, F.A.R., Bezerra-Neto, J.F., 2017. Partitioning of the diffuse attenuation coefficient for photosynthetically available irradiance in a deep dendritic tropical lake. An. Acad. Bras Cienc. 89, 469–489.

Brothers, S., Köhler, J., Attermeyer, K., Grossart, H.P., Mehner, T., Meyer, N., Scharnweber, K., Hilt, S., 2014. A feedback loop links brownification and anoxia in a temperate, shallow lake. Limnol. Oceanogr. 59, 1388–1398.

Brothers, S., Vadeboncoeur, Y., Sibley, P., 2017. A decline in benthic algal production may explain recent hypoxic events in Lake Erie's central basin. J. Great Lakes Res. 43, 73–78.

Carrick, H.J., Moon, J.B., Gaylord, B.F., 2005. Phytoplankton dynamics and hypoxia in lake erie: a hypothesis concerning benthic-pelagic coupling in the Central Basin. J. Great Lakes Res. 31, 111–124.

Chen, Z., Doering, P.H., Ashton, M., Orlando, B.A., 2014. Mixing behavior of colored dissolved organic matter and its potential ecological implication in the caloosahatchee river estuary, Florida. Estuaries Coasts 38, 1706–1718.

Chen, C., Beardsley, R.C., Cowles, G., Qi, J., Lai, Z., Gao, G., Stuebe, D., Xu, Q., Xue, P., Ge, J., Hu, S., Rubao, J., Tian, R., Huang, H., Wu, L., Lin, H., Sun, Y., Zhao, L., 2013. An unstructured grid, finite-volume community ocean model FVCOM user manual, 4th ed, p. 416.

Cheng, N., 1997. Simplified settling velocity formula for sediment particle. J. Hydraul. Eng. 123, 149–152.

Christian, D., Sheng, Y.P., 2003. Relative influence of various water quality parameters on light attenuation in Indian River Lagoon. Estuar. Coast. Shelf Sci. 57, 961–971.

CIGLR and NOAA-GLERL, 2019. Physical, chemical, and biological water quality monitoring data to support detection of Harmful Algal Blooms (HABs) in western Lake Erie, collected by the Great Lakes Environmental Research Laboratory and the Cooperative Institute for Great Lakes Research since 2012. NOAA National Centers for Environmental Information.

Depew, D.C., Guildford, S.J., Smith, R.E.H., 2006. Nearshore-offshore comparison of chlorophyll a and phytoplankton production in the dreissenid-colonized eastern basin of Lake Erie. Can. J. Fish. Aquat. Sci. 63, 1115–1129.

Effler, S.W., Peng, F., O'Donnell, D.M., Strait, C., 2013. The backscattering coefficient and its components in the Great Lakes: a review and synthesis. J. Great Lakes Res. 39, 108–122.

Environment and Climate Change Canada (ECCC), 2012. Nearshore Nuisance Benthic Algae Data (2012-). Environment and Climate Change Canada (ECCC) Data Catalogue Accessed on 11/17/2021. https://data-donnees.ec.gc.ca/data/substances/monitor/great-lakes-water-quality-monitoring-and-aquatic-ecosystem-health-data/nearshore-nuisance-benthic-algae-data-2012/?lang=en.

Fahnenstiel, G.L., Chandler, J.F., Carrick, H.J., Scavia, D., 1989. Photosynthetic characteristics of phytoplankton communities in Lakes Huron and Michigan: P-I parameters and end-Products. J. Great Lakes Res. 15, 394–407.

Fahnenstiel, G.L., Sayers, M.J., Shuchman, R.A., Yousef, F., Pothoven, S.A., 2016. Lake-wide phytoplankton production and abundance in the Upper Great Lakes: 2010–2013. J. Great Lakes Res. 42, 619–629.

Faithfull, C.L., Wenzel, A., Vrede, T., Bergström, A.K., 2011. Testing the light : nutrient hypothesis in an oligotrophic boreal lake. Ecosphere 2.

Galperin, B., Kantha, L.H., Hassid, S., Rosati, A., 1988. A quasi-equilibrium turbulent energy model for geophysical flows. J. Atmos. Sci. 45, 55–62.

Ge, J., Shen, F., Guo, W., Chen, C., Ding, P., 2015. Estimation of critical shear stress for erosion in the Changjiang Estuary: a synergy research of observation, GOCI sensing and modeling. J. Geophys. Res. Oceans 120, 8439–8465.

Ge, J., Torres, R., Chen, C., Liu, J., Xu, Y., Bellerby, R., Shen, F., Bruggeman, J., Ding, P., 2020. Influence of suspended sediment front on nutrients and phytoplankton dynamics off the Changjiang Estuary: a FVCOM-ERSEM coupled model experiment. J. Mar. Syst. 204.

Gerea, M., Pérez, G.L., Unrein, F., Soto Cárdenas, C., Morris, D., Queimaliños, C., 2016. CDOM and the underwater light climate in two shallow North Patagonian lakes: evaluating the effects on nano and microphytoplankton community structure. Aquat. Sci. 79, 231–248.

Gregg, W.W., Rousseaux, C.S., 2016. Directional and spectral irradiance in ocean models: effects on simulated global phytoplankton, nutrients, and primary production. Front. Marine Sci. 3.

Hansen, A.G., Beauchamp, D.A., Schoen, E.R., 2013. Visual prey detection responses of piscivorous trout and salmon: effects of light, turbidity, and prey size. Trans. Am. Fish. Soc. 142, 854–867.

Hawley, N., Eadie, B.J., 2007. Observations of sediment transport in Lake Erie during the winter of 2004–2005. 33, 816-827.

Hawley, N., Lesht, B.M., 1992. Sediment resuspension in Lake St. Clair. Limnology and Oceanography 37, 1720–1737.

Hawley, N., Redder, T., Beletsky, R., Verhamme, E., Beletsky, D., DePinto, J.V., 2014. Sediment resuspension in Saginaw Bay. J. Great Lakes Res. 40, 18–27.

Higgins, S.N., Hecky, R.E., Guildford, S.J., 2005. Modeling the growth, biomass, and tissue phosphorus concentration of cladophora glomerata in eastern lake erie: model description and field testing. J. Great Lakes Res. 31, 439–455.

Hu, H., van der Westhuysen, A.J., Chu, P., Fujisaki-Manome, A., 2021. Predicting Lake Erie wave heights and periods using XGBoost and LSTM. Ocean Model. 164.

Huisman, J., Sharples, J., Stroom, J.M., Visser, P.M., Kardinaal, W.E.A., Verspagen, J.M. H., Sommeijer, B., 2004. Changes in turbulent mixing shift competition for light between phytoplankton species. Ecology 85, 2960–2970.

International Field Year for Lake Erie (IFYLE), n.d. NOAA Great Lakes Environmental Research Laboratory. Accessed on 11/11/2021. https://www.glerl.noaa.gov/res/projects/ifyle/.

Jassby, A.D., Platt, T., 1976. Mathematical formulation of the relationship between photosynthesis and light for phytoplankton. Limnol. Oceanogr. 21, 540–547.

Jerome, J.H., Bukata, R.P., Bruton, J.E., 1983. Spectral Attenuation and Irradiance in the Laurentian Great Lakes. J. Great Lakes Res. 9, 60–68.

Ji, R., Chen, C., Budd, J.W., Schwab, D.J., Beletsky, D., Fahnenstiel, G.L., Johengen, T.H., Vanderploeg, H., Eadie, B., Cotner, J., Gardner, W., Bundy, M., 2002. Influences of suspended sediments on the ecosystem in Lake Michigan: a 3-D coupled bio-physical modeling experiment. Ecol. Model. 152, 169–190.

Jokela, A., Arnott, S.E., Beisner, B.E., 2013. Influence of light on the foraging impact of an introduced predatory cladoceran, Bythotrephes longimanus. Freshw. Biol. 58, 1946–1957.

Kelley, J.G.W., Chen, Y., Anderson, E.J., Lang, G.A., Xu, J., 2018. Upgrade of NOS lake erie operational forecast system (LEOFS) to FVCOM: model development and hindcast skill assessment, NOAA technical memorandum NOS CS 40. National Oceanic and Atmospheric. Administration.

Khazaei, B., Bravo, H.R., Anderson, E.J., Klump, J.V., 2021. Development of a physically based sediment transport model for green bay, Lake Michigan. J. Geophys. Res. Oceans 126.

Lang, G.A., Fahnenstiel, G., 1996. Great Lakes primary production model: methodology and use, NOAA Tech. Memo. ERL GLERL-90. NOAA Great Lakes Environmental Research Laboratory, Ann Arbor, MI.

Lashaway, A.R., Carrick, H.J., 2010. Effects of light, temperature and habitat quality on meroplanktonic diatom rejuvenation in Lake Erie: implications for seasonal hypoxia. J. Plankton Res. 32, 479–490.

Lee, Z.-P., Du, K.-P., Arnone, R., 2005. A model for the diffuse attenuation coefficient of downwelling irradiance. J. Geophys. Res. 110.

Leon, L.F., Smith, R. E., Romero, J. R., Hecky, R. E., 2006. Lake Erie Hypoxia Simulations with ELCOM-CAEDYM.

Leon, L.F., Smith, R.E.H., Hipsey, M.R., Bocaniov, S.A., Higgins, S.N., Hecky, R.E., Antenucci, J.P., Imberger, J.A., Guildford, S.J., 2011. Application of a 3D hydrodynamic–biological model for seasonal and spatial dynamics of water quality and phytoplankton in Lake Erie. J. Great Lakes Res. 37, 41–53.

Limnotech, 2021. Development, Calibration, and Application of a Lake Erie Ecosystem Model. Limnotech, Ann Arbor, MI.

Lin, S., Boegman, L., Valipour, R., Bouffard, D., Ackerman, J.D., Zhao, Y., 2021. Three-dimensional modeling of sediment resuspension in a large shallow lake. J. Great Lakes Res.

Liu, X., Chen, L., Zhang, G., Zhang, J., Wu, Y., Ju, H., 2021. Spatiotemporal dynamics of succession and growth limitation of phytoplankton for nutrients and light in a large shallow lake. Water Res 194, 116910.

Liu, Y., Yang, W., Leon, L., Wong, I., McCrimmon, C., Dove, A., Fong, P., 2016. Hydrologic modeling and evaluation of Best Management Practice scenarios for the Grand River watershed in Southern Ontario. J. Great Lakes Res. 42, 1289–1301.

Lund-Hansen, L.C., 2004. Diffuse attenuation coefficients Kd(PAR) at the estuarine North Sea-Baltic Sea transition: time-series, partitioning, absorption, and scattering. Estuar. Coast. Shelf Sci. 61, 251–259.

Morel, A., 1988. Optical Modeling of the Upper Ocean in Relation to Its Biogenous Matter Content (case I Waters). 93, 10749–10768.

Moriarty, J.M., Friedrichs, M.A.M., Harris, C.K., 2021. Seabed resuspension in the chesapeake bay: implications for biogeochemical cycling and hypoxia. Estuaries Coast 44, 103–122.

Morris, D.P., Zagarese, H., Williamson, C.E., Balseiro, E.G., Hargreaves, B.R., Modenutti, B., Moeller, R., Queimalinos, C., 1995. The attenuation of solar UV radiation in lakes and the role of dissolved organic carbon. Limnol. Oceanogr. 40, 1381–1391.

Niu, Q., Xia, M., Ludsin, S.A., Chu, P.Y., Mason, D.M., Rutherford, E.S., 2018. High-turbidity events in Western Lake Erie during ice-free cycles: contributions of river-loaded vs. resuspended sediments. Limnol. Oceanogr. 63, 2545–2562.

NOAA-GLERL and CIGLR. Physical, chemical, and biological water quality observation data at multiple levels from an array of fixed moorings to support hypoxia research in the central basin of Lake Erie, Great Lakes region collected by the NOAA Great Lakes Environmental Research Laboratory and the Cooperative Institute for Great Lakes Research, University of Michigan, since 2017. NOAA National Centers for Environmental Information, 2020. https://doi.org/10.25921/qd27-bj97.

NOAA CoastWatch, 2023. NOAA CoastWatch Great Lakes Regional Node Accessed on 12/14/2020. https://coastwatch.glerl.noaa.gov/satellite-data-products/.

Pangle, K.L., Ramcharan, C., Peacor, S.D., 2009. Light-dependent predation by the invertebrate planktivore Bythotrephes longimanus. Can. J. Fish. Aquat. Sci. 66, 1748–1757.

Perkins, M., Effler, S.W., Peng, F., O'Donnell, D.M., Strait, C., 2013. Light-absorbing components in the Great Lakes. J. Great Lakes Res. 39, 123–136.

Pilla, R.M., Couture, R.M., 2021. Attenuation of photosynthetically active radiation and ultraviolet radiation in response to changing dissolved organic carbon in browning lakes: Modeling and parametrization. Limnol. Oceanogr. 66, 2278–2289.

Prater, C., Frost, P.C., Howell, E.T., Watson, S.B., Zastepa, A., King, S.S.E., Vogt, R.J., Xenopoulos, M.A., 2018. Variation in particulate C : N : P stoichiometry across the Lake Erie watershed from tributaries to its outflow. Limnol. Oceanogr. 62. S1, S1940S206 https://doi.org/10.1002/lno.10628.

Riseng, C.M., Wehrly, K.E., Wang, L., Rutherford, E.S., McKenna, J.E., Johnson, L.B., Mason, L.A., Castiglione, C., Hollenhorst, T.P., Sparks-Jackson, B.L., Sowa, S.P., 2018. Ecosystem classification and mapping of the Laurentian Great Lakes. Can. J. Fish. Aquat. Sci. 75, 1693–1712.

Robertson, D.M., Hubbard, L.E., Lorenz, D.L., Sullivan, D.J., 2018. A surrogate regression approach for computing continuous loads for the tributary nutrient and sediment monitoring program on the Great Lakes. J. Great Lakes Res. 44, 26–42.

Rowe, M.D., Anderson, E.J., Vanderploeg, H.A., Pothoven, S.A., Elgin, A.K., Wang, J., Yousef, F., 2017. Influence of invasive quagga mussels, phosphorus loads, and climate on spatial and temporal patterns of productivity in Lake Michigan: a biophysical modeling study. Limnol. Oceanogr. 62, 2629–2649.

Rowe, M.D., Anderson, E.J., Beletsky, D., Stow, C.A., Moegling, S.D., Chaffin, J.D., May, J.C., Collingsworth, P.D., Jabbari, A., Ackerman, J.D., 2019. Coastal upwelling influences hypoxia spatial patterns and nearshore dynamics in Lake Erie. J. Geophys. Res. Oceans.

Schwab, D.J., Beletsky, D., 1998. Lake Michigan Mass Balance Study: Hydrodynamic Modeling Project, ERL GLERL-108. NOAA Great Lakes Environmental Research Laboratory, p. 53.

Shuchman, R.A., Leshkevich, G., Sayers, M.J., Johengen, T.H., Brooks, C.N., Pozdnyakov, D., 2013. An algorithm to retrieve chlorophyll, dissolved organic carbon, and suspended minerals from Great Lakes satellite data. J. Great Lakes Res. 39, 14–33.

Smagorinsky, J., 1963. General circulation experiments with the primitive equations. Mon. Weather Rev. 91, 99–164.

Smith, R.E.H., Allen, C.D., Charlton, M.N., 2004. Dissolved organic matter and ultraviolet radiation penetration in the laurentian great lakes and tributary waters. J. Great Lakes Res. 30, 367–380.

Smith, R.C., Baker, K.S., 1978. The bio-optical state of ocean waters and remote sensing. Limnol. Oceanogr. 23, 247–259.

Son, S., Wang, M., 2015. Diffuse attenuation coefficient of the photosynthetically available radiation Kd(PAR) for global open ocean and coastal waters. Remote Sens. Environ. 159, 250–258.

Song, K., Ma, J., Wen, Z., Fang, C., Shang, Y., Zhao, Y., Wang, M., Du, J., 2017. Remote estimation of Kd (PAR) using MODIS and Landsat imagery for turbid inland waters in Northeast China. ISPRS J. Photogramm. Remote Sens. 123, 159–172.

Stow, C.A., Reckhow, K.H., Qian, S.S., 2006. A Bayesian approach to retransformation bias in transformed regression. Ecology 87, 1472–1477.

Stow, C.A., Dyble, J., Kashian, D.R., Johengen, T.H., Winslow, K.P., Peacor, S.D., Francoeur, S.N., Burtner, A.M., Palladino, D., Morehead, N., Gossiaux, D., Cha, Y., Qian, S.S., Miller, D., 2020. Physical, chemical, and biological water quality data and CTD casts collected from small boats in Saginaw Bay, Lake Huron in the Great Lakes region from 2008–05-12 to 2010–10-13 (NCEI Accession 0220469). NOAA National Centers for Environmental. Information. https://www.ncei.noaa.gov/archive/accession/0220469.

Stow, C.A., Rowe, M.D., Godwin, C.M., Mason, L.A., Alsip, P.J., Kraus, R.T., Johengen, T. H., Constant, S.A., 2023. Lake Erie hypoxia spatial and temporal dynamics present challenges for assessing progress toward water quality goals. J. Great Lakes Res.

Stumpf, R.P., Wynne, T.T., Baker, D.B., Fahnenstiel, G.L., 2012. Interannual variability of cyanobacterial blooms in Lake Erie. PLoS One 7, e42444.

Sullivan, C.R., Gurdak, D.J., 2022. Building a CSMI database: experiences from the Lake Ontario 2018 CSMI Field Year. J. Great Lakes Res. 48, 434–440.

Tan, X., Zhang, D., Duan, Z., Parajuli, K., Hu, J., 2020. Effects of light color on interspecific competition between Microcystis aeruginosa and Chlorella pyrenoidosa in batch experiment. Environ Sci Pollut Res Int 27, 344–352.

Urabe, J., Kyle, M., Makino, W., Yoshida, T., Andersen, T., Elser, J.J., 2002. Reduced light increases herbivore production due to stoichiometric effects of light/nutrient balance. Ecology 83.

Valipour, R., León, L.F., Depew, D., Dove, A., Rao, Y.R., 2016. High-resolution modeling for development of nearshore ecosystem objectives in eastern Lake Erie. J. Great Lakes Res. 42, 1241–1251.

Valipour, R., Boegman, L., Bouffard, D., Rao, Y.R., 2017. Sediment resuspension mechanisms and their contributions to high-turbidity events in a large lake. Limnol. Oceanogr. 62, 1045–1065.

Van Prooijen, B.C., Winterwerp, J.C., 2010. A stochastic formulation for erosion of cohesive sediments. J. Geophys. Res. 115.

Verhamme, E.M., Redder, T.M., Schlea, D.A., Grush, J., Bratton, J.F., DePinto, J.V., 2016. Development of the Western Lake Erie Ecosystem Model (WLEEM): application to connect phosphorus loads to cyanobacteria biomass. J. Great Lakes Res. 42, 1193–1205.

Weiskerger, C.J., Rowe, M.D., Stow, C.A., Stuart, D., Johengen, T., 2018. Application of the beer-lambert model to attenuation of photosynthetically active radiation in a shallow, Eutrophic Lake. Water Resour. Res. 54, 8952–8962.

Wick, M., Cotter, A., McKinney, P., Hollenhorst, T., Opseth, A., Pawlowski, M., Trebitz, A., in press. Lake Huron 2017 CSMI Ship & Glider Water Quality Summary. U.S. EPA Office of Research and Development, Great Lakes Toxicology and Ecology Division, p. 29. https://greatlakescsmi.org/csmi/wp-content/uploads/2023/10/2017-Lake-Huron-Cooperative-Science-and-Monitoring-Initiative-CSMI-Report-FINAL-web.pdf.

Wynne, T.T., Stumpf, R.P., Tomlinson, M.C., Schwab, D.J., Watabayashi, G.Y., Christensen, J.D., 2011. Estimating cyanobacterial bloom transport by coupling remotely sensed imagery and a hydrodynamic model. Ecol Appl 21, 2709–2721.

Yamaguchi, H., Katahira, R., Ichimi, K., Tada, K., 2013. Optically active components and light attenuation in an offshore station of Harima Sound, eastern Seto Inland Sea, Japan. Hydrobiologia 714, 49–59.

Yang, H., Xie, P., Xing, Y., Ni, L., Guo, H., 2005. Attenuation of photosynthetically available radiation by chlorophyll, chromophoric dissolved organic matter, and tripton in Lake Donghu, China. J. Freshwater Ecol. 20, 575–581.

Zhang, Y., Zhang, B., Ma, R., Feng, S., Le, C., 2007. Optically active substances and their contributions to the underwater light climate in Lake Taihu, a large shallow lake in China. Fundam. Appl. Limnol. 170, 11–19.

Zhou, Y., Obenour, D.R., Scavia, D., Johengen, T.H., Michalak, A.M., 2013. Spatial and temporal trends in Lake Erie hypoxia, 1987–2007. Environ Sci Technol 47, 899–905.